CATO-2 Deliverable WP 3.3 – D18

Report/paper documenting: Sorption and CT experiments on the transport and sealing properties of samples relevant to key sites

Prepared by: F.C. Schoemaker (TUD)
Auke Barnhoorn (TUD)
Patrick van Hemert (TUD)

Reviewed by: Auke Barnhoorn (TUD)

Approved by: (CATO-2 Director)

1 Executive Summary (restricted)

The long term integrity and sealing property of the cap rock associated with CO_2 -exposure have been established by the following laboratory experiments: manometric sorption experiments, pendant drop wettability experiments, capillary pressure drainage and imbibition experiments, and rock mechanical experiments.

Experiments have been conducted with selected shale samples from the key site, well Q4-8, and the more readily available Mercian mud from Great-Britain and black shale from Belgium as analogue samples. Limited CT scans have also been performed.

The wettability of the shale determines its likelihood for CO_2 leakage. The lower the affinity of the shale for CO_2 , the lower the likelihood for leakage. CO_2-water-shale contact angle measurements demonstrate that the shales from well Q4-8 are water-wet at pressures below 120 bar and thus pose minimal risk for leakage. However, the affinity for CO_2 may increase with higher salt concentrations and higher pressures. Additional experiments are required to evaluate this risk.

Another indicator for the likelihood of leakage through a shale is its capillary pressure of CO_2–water drainage and imbibition. The lower the capillary pressure, the higher the likelihood of leakage. Present experiments on unconsolidated shales with high porosities (~46%) show low capillary pressure, thus a likelihood of leakage. In subsequent experiments on consolidated low-porosity shales much higher capillary pressures are expected, i.e. minimal leakage. The laboratory measurements of capillary pressure on unconsolidated shale (<10 mbar at 11 bar pressures) are lower than the previously reported capillary pressure of unconsolidated sands and exhibit qualitative similar drainage and imbibition behaviour as unconsolidated sands. Future consolidated shale capillary pressure data will provide an upper limit of leakage for *in situ* conditions of the CO_2 sequestration reservoirs in the Dutch subsurface.

The sorption experiments show that sorption equilibrium of CO_2 on shales is attained in tens of hours, which is considerably faster than sorption of CO_2 on coals. These results indicate that the assumption of instantaneous sorption equilibrium of CO_2 on shales in computer modelling of CO_2 sequestration in the subsurface is an acceptable approximation. Long-term alterations in terms of sorption processes in shales are expected to have a low probability.

Rock mechanical experiments on shales from well Q4-8 show that the shales have an unconfined compressive peak strength of ~110 MPa, which is in line with literature values of other low-porosity sedimentary rock types. Indeed, the sand (e.g. quartz grains) interlayed between the shale intervals increases the unconfined compressive peak strength of the shale sample considerably. Information on the porosities and mineralogical composition of the shale cap rocks is vital to predict its long term integrity.

Distribution List

(this section shows the initial distribution list)

External	Copies	Internal	Copies
		Program Office CATO-2	electronic
		Authors & WP3.3 partners & stakeholders	electronic

Document Change Record

(this section shows the historical versions, with a short description of the updates)

Version	Nr of pages	Short description of change	Pages
2011-12-15	52	Initial report by TUD	1-52

Table of Content

2 Applicable/Reference documents and Abbreviations

2.1 Applicable Documents

(Applicable Documents, including their version, are documents that are the "legal" basis to the work performed)

	Title	Doc nr	Version
~~AD-01a~~	~~Beschikking (Subsidieverlening CATO-2 programma verplichtingnummer 1-6843~~	~~ET/ED/9078040~~	~~2009.07.09~~
~~AD-01b~~	~~Wijzigingsaanvraag op subsidieverlening CATO-2 programma verplichtingennr. 1-6843~~	~~CCS/10066253~~	~~2010.05.11~~
~~AD-01c~~	~~Aanvraag uitstel CATO-2a verplichtingennr. 1-6843~~	~~ETM/10128722~~	~~2010.09.02~~
AD-01d	Toezegging CATO-2b	FES10036GXDU	2010.08.05
AD-01f	Besluit wijziging project CATO2b	FES1003AQ1FU	2010.09.21
AD-02a	Consortium Agreement	CATO-2-CA	2009.09.07
AD-02b	CATO-2 Consortium Agreement	CATO-2-CA	2010.09.09
~~AD-03a~~	~~Program Plan 2009~~	~~CATO2-WP0.A-D.03~~	~~2009.09.17~~
~~AD-03b~~	~~Program Plan 2010~~	~~CATO2-WP0.A-D.03~~	~~2010.09.30~~
AD-03c	Program Plan 2011	CATO2-WP0.A-D.03	2010.12.07

2.2 Reference Documents

(Reference Documents are referred to in the document)

	Title	Doc nr	Version/issue	Date

2.3 Abbreviations

(this refers to abbreviations used in this document)

3 General Text

3.1 Introduction

Since the past decade, the interest for research on shales has increased within the petroleum industry. Shales form the cap layer of traditional hydrocarbon reservoirs, and they are also the location in which natural (shale) gas can be found. For the storage of CO_2 in reservoirs, coal seams or aquifers the seal often consists of shale material. In this report, the latter is the primary focus of our attention. The injection of high pressure CO_2 in the underground can have lots of consequences. It will change stresses in the caprock layer, even increasing the possibility of endangering the overburden integrity of the caprock. These effects are amongst others poro-elastic effects, which are caused by changes in pore fluid pressure, thermo-elastic effects caused by changes in the pore fluid temperature, dissolution-precipitation reactions caused by changes in pore fluid chemistry and desiccation effects caused by water uptake due to the injection of CO_2 (CATO WP3.3 web report [CATO2-WP3.3, 2010]).

This report describes the sorption behaviour of shale rocks using various techniques including capillary pressure experiments of CO_2-water-shale systems,CO_2-water-clay contact angle measurements and the sorption behaviour of CO_2 on shales. The sorption and wettability data reported here can be used to determine the long term of cap-rock integrity of shales as well as possible leakage of CO_2 through shale cap rocks. Rock mechanical properties of selected shale samples from the key site well Q4-8 are included in the report. Limited CT work has also been performed.

Capillary pressure can be important for the long term integrity of the rock. At Delft university *Plug [2007]* is one of the pioneers with an experimental set-up for measuring capillary pressure, for elevated temperature and pressure [*Hemert, 2010*]. Also our attention is directed towards the adsorption capacity of the caprock, Saikat and van Hemert have pioneered with this setup, that is capable of measuring the sorption capacity up to high pressures and temperatures. Contact angle measurements of CO_2 in shales describe the wettability of the systems, whereby water wet conditions favour long term storage of CO_2 and the integrity of shales whereas intermediate-wet conditions may lead to leakage of CO_2 through shales.

3.2 Material background and applied method

The caprock of the reservoir under consideration, has been formed in the Trias period. The reservoir area is located in the North Sea, on the continental shelf. The first layers of the Trias in this area are often located on top of material from the Carbon period or material from the late Permian period. In the early periods of Trias, 4 layers can be distinguished in this area, of which the three, Volpriehausen, Detfurth and the Hardegsen formation are known as the main Buntsandstein subgroup. This group has a maximum thickness of 650 m in the centre of the North Sea and is rather homogenous in composition [*Berendsen, 2011*]. It is an ideal reservoir material and will become the reservoir in which the CO_2 can be stored.
During the middle part of the Trias period, the sea level rose and the Netherlands and North Sea were part of the German Basin, within the Thetys Ocean. This part of the sea was rather shallow, the upper part of the Buntsandstein subgroup is covered by material of the Upper-German Trias group. This material consists of sandstone, claystone, chalk, dolomite, and evaporite (see also the XRD and XRF results, which will be discussed hereafter). Also here four layers are distinguished, Solling, Röt, Muschelchalk and the Keuper formation. Of which the first two, together are known as the upper Buntsandstein formation. The content among the layers is specified as follows. The Solling formation consists of claystone, the Röt formation of a salt layer (evaporites), which is up to 300 m thick in the North Sea. The Chalkstone is found in the Muschelchalk formation with occasionally some evaporites (maximum thickness is up to 500 m) [*Berendsen, 2011; TNO National Geological Survey, 2004*]. XRF and XRD data of the Muschelkalk, Sölling Rot and Mercian mud are reported in the Appendix.
During the last part of Trias, sediments originated from what is now Scandinavia, are deposited in the North Sea area. It consists of clays as well as sandstones, with occasionally anhydrites, salt, gypsum and dolomites. This group of materials is known as the Keuper formation.
Additional material, from an shallow source in the Earth (almost toplayer material from a couple of meters depth) can be seen as an equivalent material to the Solling, Röt and Muschelchalk and is also used in this research. It is easier to obtain, but is more fragile, due to its shallow location. It is from the Mercia formation. This Mercian mudstone, has been obtained in England [*TNO National Geological Survey, 2004*].

Wintershall provided us with several cores for analysis (Table 1) from well Q4-8, unfortunately a lot of this material was fractured, so consolidated material tests can only be performed on relative small samples.

Table 1 Analysed shale samples.

Location			m	M	M	cm	cm	
Q4-8	Core #2	1/2 cut	2455	2456	2456	63		Muschelchalk Röt
Q4-8	Core #2	1/2 cut	2460	2461	2461	31	19	Muschelchalk Röt/ Solling
Q4-8	Core #2	1/2 cut	2473	2474	2473,4	32		Solling claystone
Q4-8	Core #3	1/2 cut	2489	2490	2490	18		Solling claystone
Q4-A3B		1/2 cut	3308	3309	3309	32		Dethfurth
								Black shale Belgium

3.2.1 Capillary pressure analysis of the caprock

The long term integrity of the caprock is, in part, dependent on the pressure necessary for displacing originally present water by CO_2. This entrance pressure is referred to as capillary pressure and can be determined in laboratory experiments in order to ensure that the caprock is sufficiently sealing.

The objective of this study is to validate in the laboratory that the caprock shales have sufficiently high capillary pressures that the integrity of the caprock is guaranteed. Two distinct experimental approaches are being taken to measure the capillary pressure: (1) a direct measurement of the capillary pressure of the shale-H_2O-CO_2 system, (2) a measurement of the contact angle of the H_2O-CO_2-shale system from which the capillary pressure can be calculated.

The relationship between capillary pressure, P_{cap}, and contact angle is given by [*Chiquet et al, 2005*]

$$P_{CO2} - P_{H2O} = \frac{\gamma_{H2O,CO2}\cos(\theta)}{R}$$

where *R* is the maximum pore throat size, $\gamma_{H2O,CO2}$ is the interfacial tension between water and carbon dioxide, θ is the contact angle (see section 3.2.4 pendant drop cell) and P_{CO2} and P_{H2O} the CO_2 pressure and the water pressure respectively. CO_2 could possibly alter the wettability of the caprock [*Plug, 2007*]..

Capillary pressure is very dependent on the pore size distribution of the material and the saturation [*Al-Garni, 2008*]. Therefore, a wide range of grain sizes has been used.

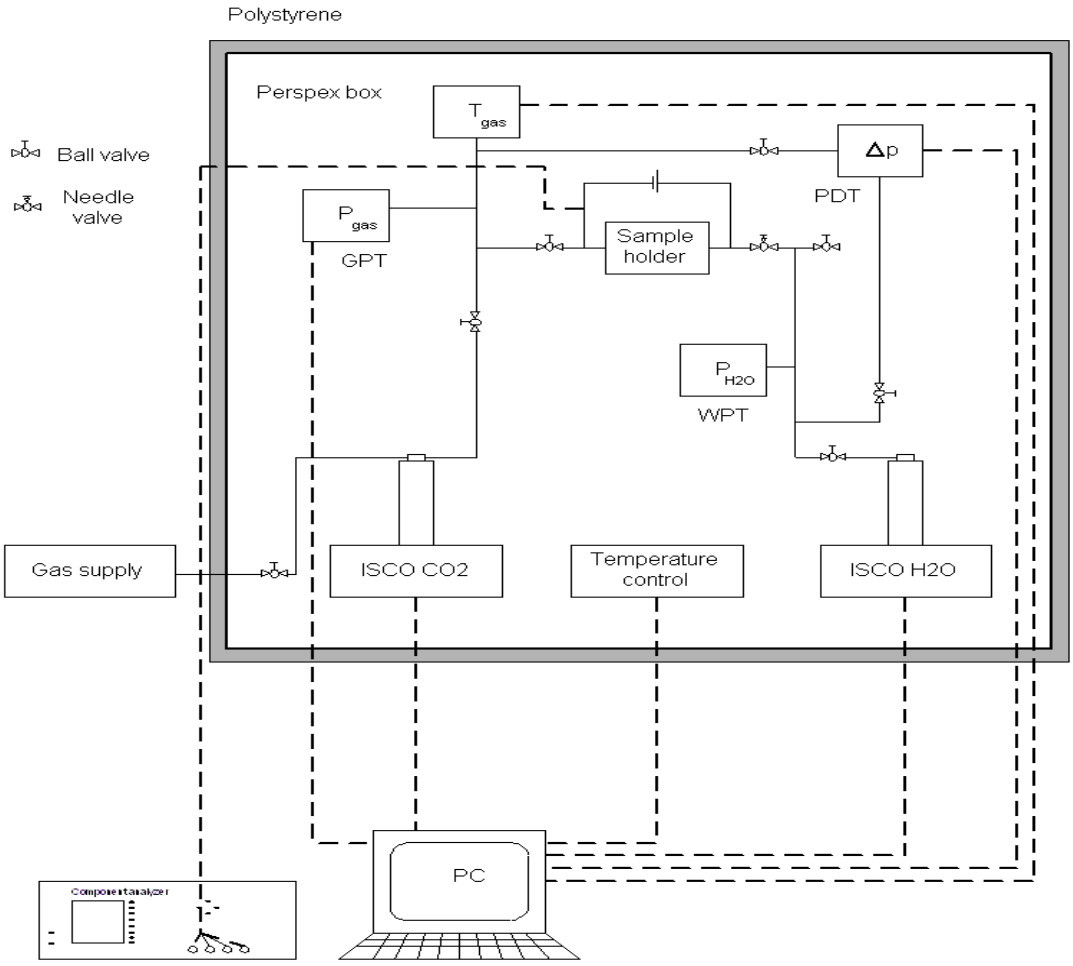

Figure 1: Schematic of the capillary pressure set-up (modified from [Plug, 2007]).

Materials and methods

The used setup, as developed by *Plug (2007)* can measure the capillary pressure behaviour for CO_2 sequestration. Static drainage and imbibition capillary pressures for CO_2 can be obtained for different pressures and temperatures [*Plug, 2007*]. The setup (Figure 1) has been used for measurements on unconsolidated samples. During a next step, also consolidated sample s will be analysed, Figure 2b (consolidated samples have

not been tested before). So far early preparations have been made to construct the sample, the applied shales have the tendency to swell and fracture (for these measurements it is necessary to maintain the structural integrity) during construction of the sample.

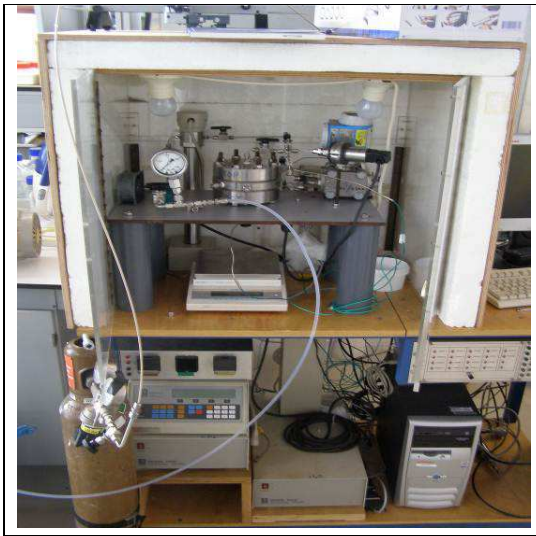

Figure 2 a & b: Capillary pressure setup and to be investigated shale sample.

From Figure 1 and 2a, it is seen that two syringe pumps are connected to the pressure cell sample holder. They are capable of operating at a constant pressure (with an accuracy of ±0.01 bar) or a constant flow rate (with an accuracy of 0.005 ml/h). Water is injected using one of the syringe pumps from the bottom (pressures above atmospheric pressure), (see figure 3, (part 2)). The other syringe pump injects the gas, e.g. CO_2 from the top of the sample (see figure 3, (part 1)).
The water pressure transducer (WPT) and the gas pressure transducer (GPT) each measure the single phase pressure. The dual phase (water gas) differential pressure is measured using the pressure difference transducer (PDT). The entire setup (see figure 2a) is located in a Perspex box which is covered by polystyrene. Using two light bulbs of 60 W the temperature can be controlled between 25°C and 40°C with an accuracy of 1 °C. During the measurements the software system has been refurbished, the previous system was outdated and not flexible.

The pressure cell sample holder, figure 3, consists out of a variety of parts. The bottom and top side consists out of stainless steel rings, which can hold pressure upto over 100 bar. The middle ring is either made of either PEEK or stainless steel. The PEEK ring is used for low pressure differences (maximum difference 45 bar) and the steel ring for higher pressures. The shale sample (black shale and in the future Solling and Röt) is located in a steel cylinder. Above and below the sample filters are located. The filters have a higher permeability than the sample. The filters are amongst others required to obtain an optimal pressure distribution. The filters have an outer seal (Viton O ring), to avoid leakage of gas and water [*Plug, 2007*] .

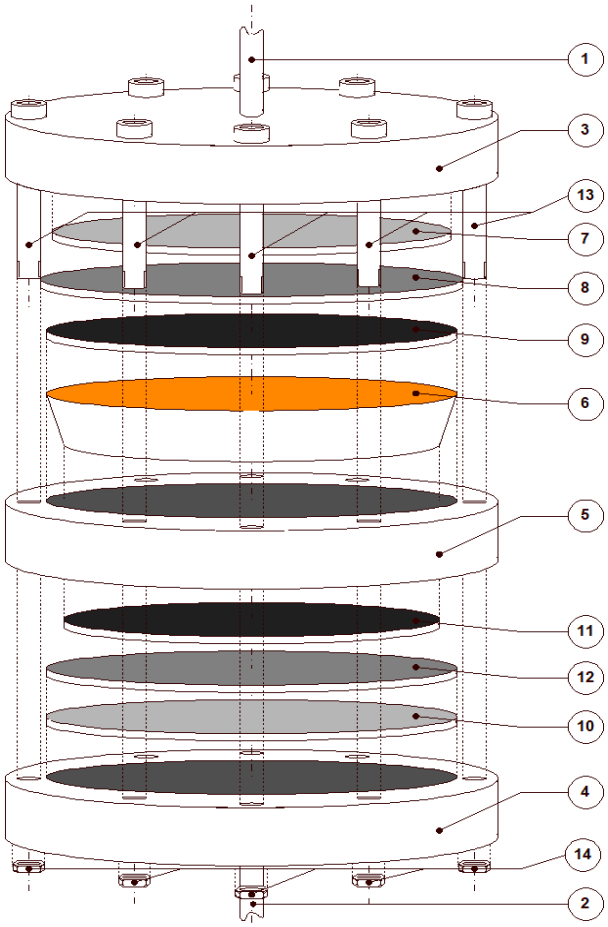

Figure 3: Exploded view capillary pressure, sample holder pressure cell.
1. Gas inlet; 2. Water inlet; 3. Top side pressure cell (stainless steel); 4. Bottom side pressure cell (stainless steel); 5. PEEK ring; 6. Clay core; 7. Porous Monel plate; 8. Porous Monel plate; 9. Nylon filter plate; 10. SIPERM plate; 11. SIPERM plate; 12 .Water-wet filter plate; 13. Bolts (stainless steel); 14. Screws. (modified from [Plug (2007)].)

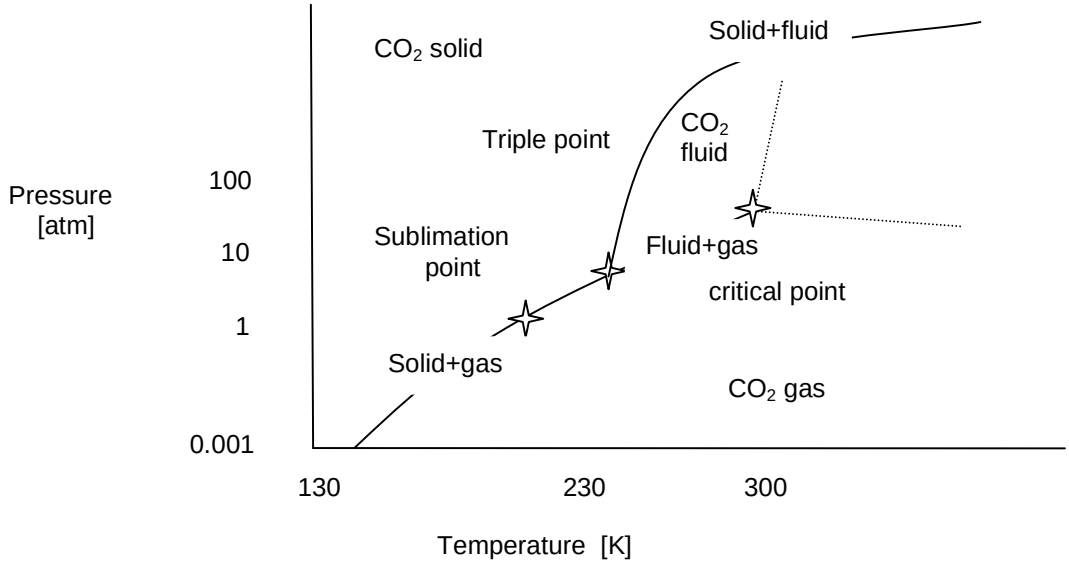

Figure 4: Phase diagram CO_2 , pressure versus temperature [modified from [Shakhashiri, 2008]]

During the measurements, the setup is first cleaned and dried. The sample is placed and the system is filled with helium for testing of leakage. After that the volume of the sample can be determined. For a detailed description see *Plug, 2007*. In our experiments, first some initial tests are performed using unconsolidated sand. The unconsolidated sand experiment reproduced the capillary behaviour reported by Plug, 2007.
After this initial testing stage, capillary behaviour during drainage and imbibition of a Belgium black shale aggregate with aggregate sizes between 0.06 mm-2mm. CO_2 and water injection rates for the black shale experiments are 1 ml/hr. The capillary pressure behaviour of shale is small (Figure 5). Black shale capillary pressure at 11 bars are lower than for unconsolidated sands. Entry pressures are in the range of a few millibars for black shales. The end of primary drainage for shales are only ~3-4 mbars higher than the shale entry pressures. Imbibition and drainage trends for shale aggregates have the same characteristics as the imbibition and drainage trends for unconsolidated sands (Plug 2007).

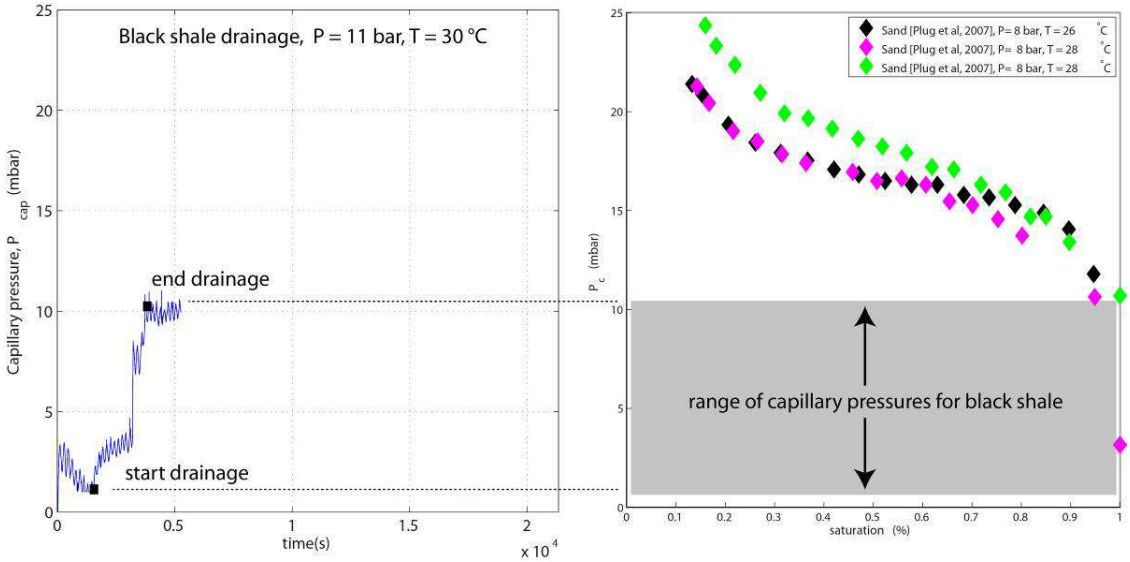

Figure 5: a) Capillary pressure drainage curve of black shale aggregates at 11 bars and 30 °C. b) Comparison with drainage curves of unconsolidated sands at much higher capillary pressures (Plug et al., 2007).

3.2.2 Pendant drop cell

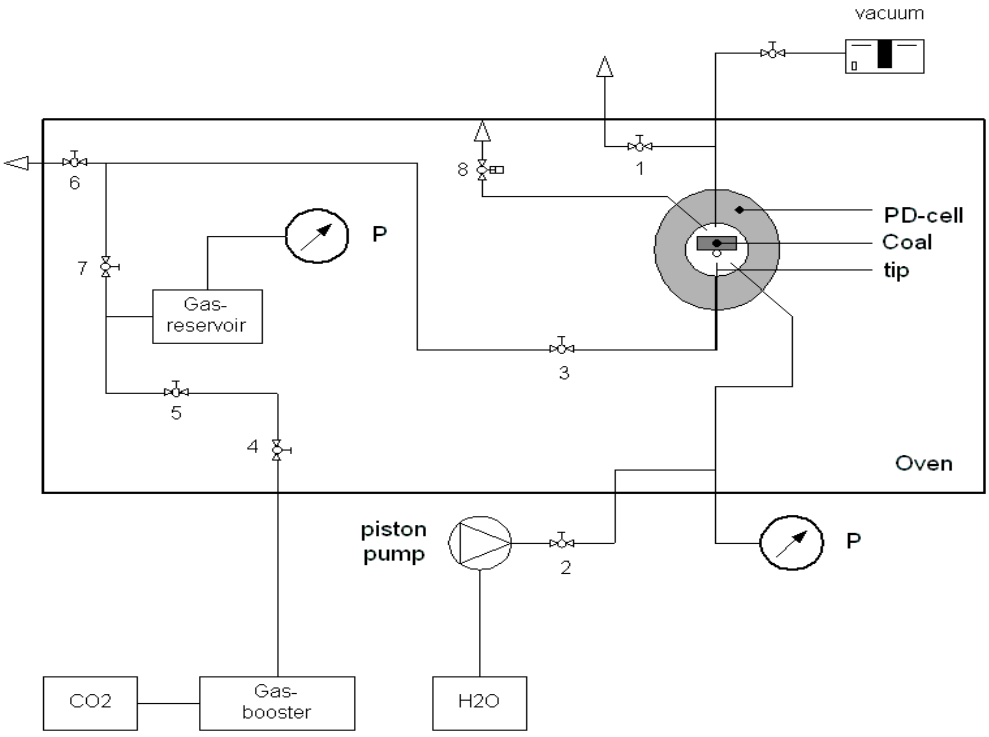

Figure 6: Schematic view of the pendant drop cell for measuring water-H2O-coal contact angles (modified from [Siemons, 2007]).

The pendant drop cell (figure 6) is based on the work of *Huygens (1990),* the setup is adapted to perform captive-bubble contact-angle measurements. This setup makes it possible to measure CO_2 water clay contact angles. The main sensor is a digital camera which records images through an endoscope. To regulate the temperature, the entire set-up is located in an insulated oven. At the start of the experiment the cell is filled with tap water in which a CO_2 bubble is injected through a capillary tube at the bottom of the set-up [*van Hemert, 2010*]. The outcome is recorded by the camera.
As shown during the derivation of the capillary pressure, the contact angle has a direct connection with the capillary pressure, see equation (3.2.3-1). For the storage capacity, several factors are of importance. These are capillary breakthrough of CO2 phase, diffusion of CO2 molecules in the cap rock and hydraulic/ thermal fracturing [*Chiquet et al, 2005*]. We consider the first effect, because the wettability (preference of a solid to be in contact with a fluid, which is directly related to the contact angle) can change under pressure. Previous measurements *by Chiquet et al, 2005* have shown that CO2 under

geological pressures can alter the wettability from water-wet to intermediate wet. Thereby making it possible that leakage occurs, especially over longer time frames (periods of several thousands of years). Although the permeability of the shale is low, carbon dioxide breakthrough can still happen. Similar to a cleat system as described by [Siemons et al, 2006] molecular diffusion will be small while for a CO2 filled system it will be larger.

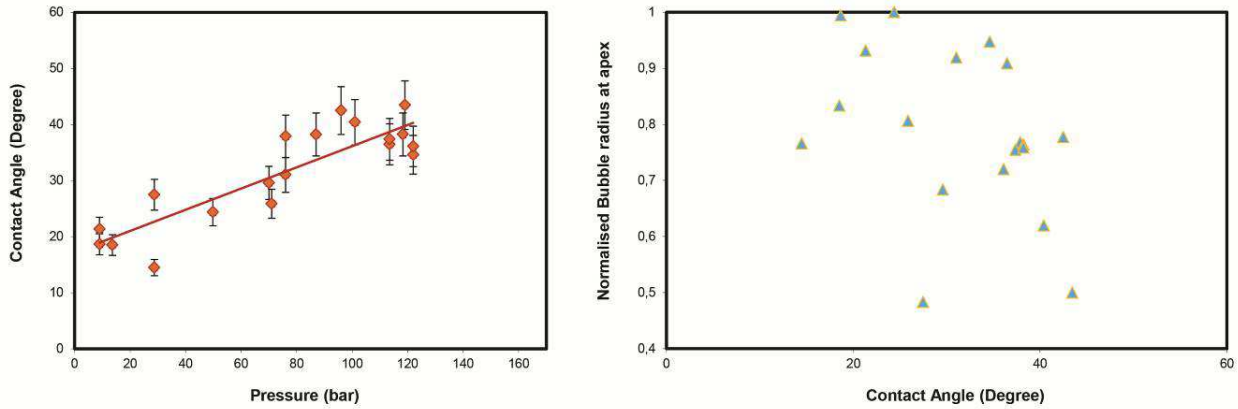

Figure 7 Contact angle dependence on pressure and bubble radius vs. contact angle in water-wet shale.

Figure 7 and 8 shows that consolidated shale from well Q4-8 at 2461m depth is water-wet since the contact angles are well below 90 °. However, the pressure dependence in black shales shows a gradual transition to more intermediate-wet configurations. High pressures (>>140 bar), i.e. large burial depths may make shales eventually intermediate-wet. The reported data from Chiquet et al. (2005) shows intermediate wet configurations at high salt concentrations and at high pressures.
The results reported here would indicate that intermediate-wet conditions and hence possible leakage of CO2 is only important at relatively high pressures, however the salt concentration of the water in the shales plays an important role too.

The contact angle vs. bubble radius (Fig.7) shows no real dependence for black shales, which is in contrast with sandstones. A clear relation between bubble radius and contact angle for water-wet sandstones is reported in the current CATO-2-WP3.2-D04 report.

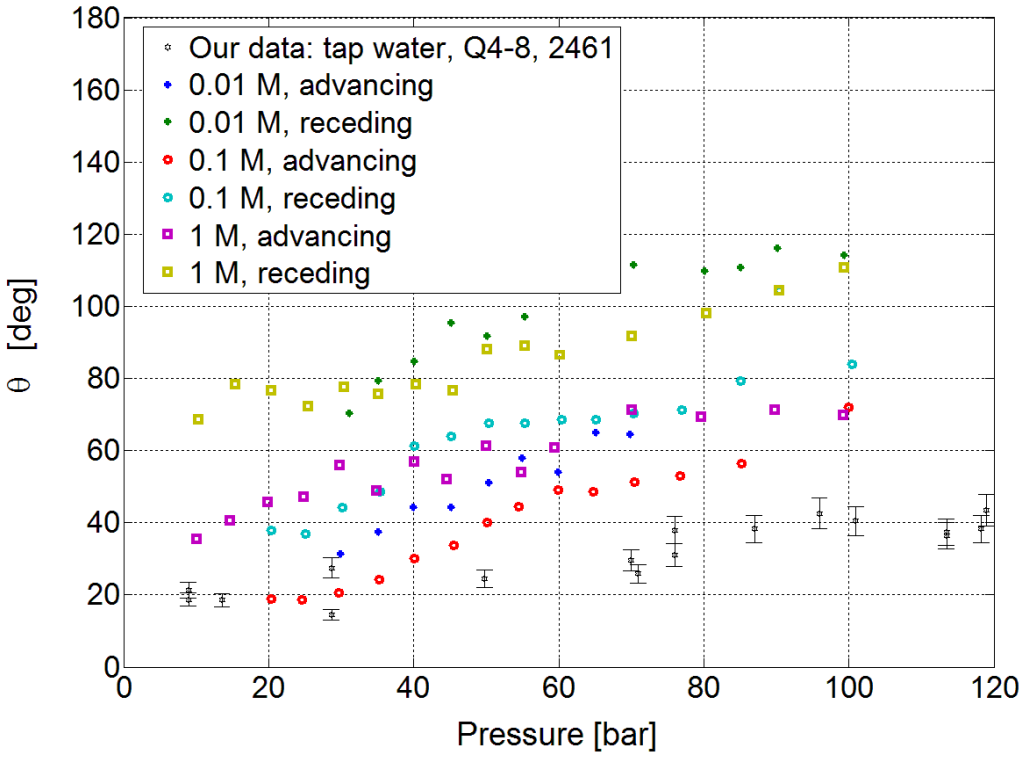

Figure 8 Advancing and receding contact angles of quartz in brines for various salt contents as measured by [Chiquet et al, 2005] compared with Q4-8, 2461m shale in tap water.

From the capillary measurements in section 3.2.1 we can see that the imbibition of shale (decreasing the amount of water saturation) and the above lying drainage curve (increasing the water saturation) indicate that the system is water-wet.

3.2.3 Manometric sorption measurements

In this experiment we consider the amount of CO_2 that can be sorbed in the cap rock. That study is considered to give us a more profound insight in the interaction between CO_2 and the cap layer.

The storage capacity of gas reservoirs for CO_2 depends on its dissolution in brine as well as on minerals and shales in the porous medium. So the sorption characteristics depend

on the composition of the shale material. Measurements on shales of various compositions are necessary to estimate the sorption in practice.

The excess sorption isotherms have been measured at a constant temperature of 318 K at pressures up to 9 MPa (90 bar). These conditions are representative of typical European in situ conditions.

Materials and methods

We have been performing measurements on Belgium black shale. In the following measurements this material will be replaced with above mentioned cap rock samples (see table 1.).

The applied measurement procedure consists of the preparation of the sample, by sieving, granulized material to a size range of 40-220 µm. Drying the sample by putting it in the oven for 24 hours. Thereafter mineral composition is determined using XRD and XRF (see the composition of black-shale here below). Finally the four experimental procedure steps are performed to obtain the sorption data (*Khosrokhavar et al, 2012*).

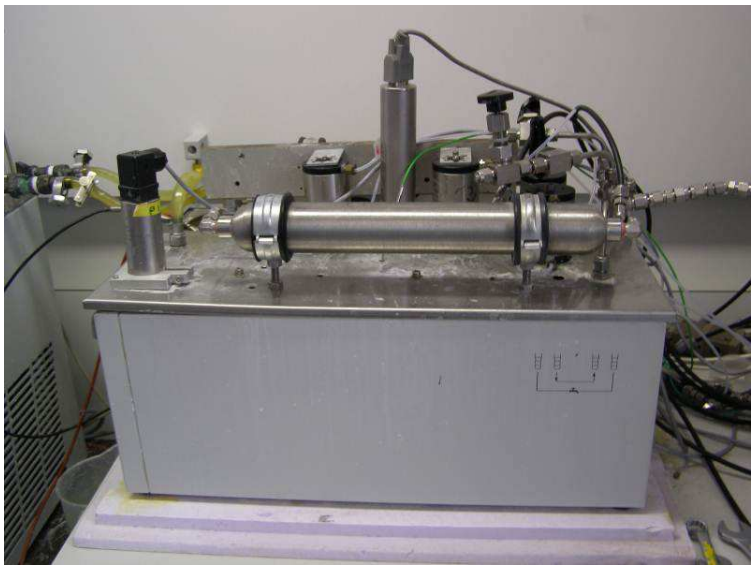

Figure 9: Manometric sorption setup.

The manometric sorption apparatus (figure 9) used in this study has previously been developed and used by *van Hemert (2009)* for determining the sorption of CO_2 on coal samples. The entire data-acquisition hard- and software have been replaced in order to decrease time necessary for an experiment. The technical schematic of the manometric setup is given in figure 10.

Following van Hemert (2009) procedure for high accuracy sorption experiments, each experiment consists of four separate consecutive steps: 1) Leak rate determination with helium; 2) determination of accessible volume by helium; 3) CO_2 sorption experiment with ~40 h as the time allotted for equilibriation ; and, 4) a repeat measurement of the accessible volume by helium. The repeat measurement is performed to confirm that the volume changes of the sample are minimal as changes in volume have a profound effect on the sorption measurements.

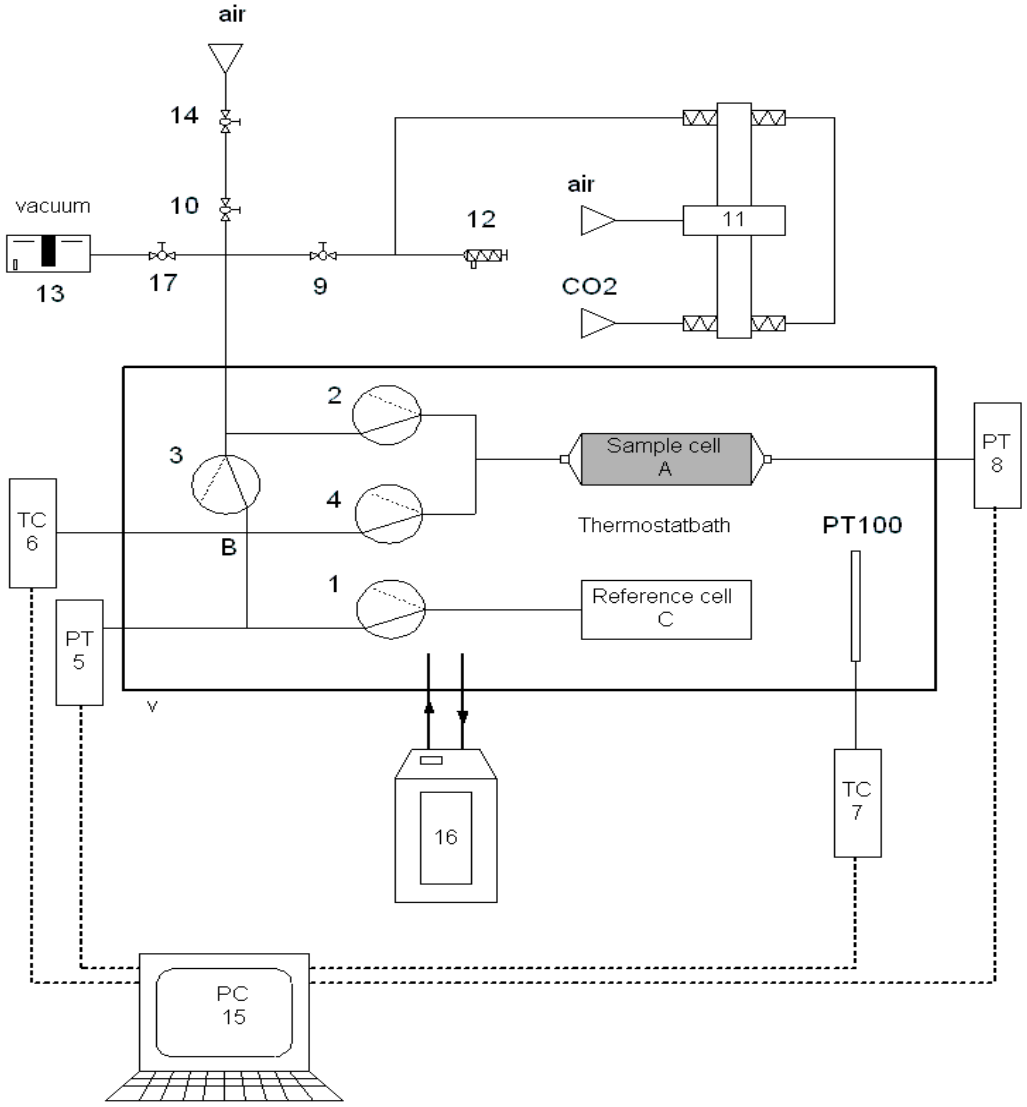

Figure 10: Schematic of manometric sorption setup (modified from [van Hemert, 2009]). In the sample cell (A) unconsolidated caprock material is located (content is ±76 cc and ±78 cc). Reference cell (C), is similar to sample cell (A), besides that there is additional space which only consists of tubing (B). The elements 1 upto 4 in figure 5 are air actuated valves. The main sensors for analysing the system are the pressure transmitters 5 and 8 and the temperature sensors 6 and 7. Ball valves, elements 9, 10 and 17 give the system access to a vacuum system 13, to compressed air and a CO_2 input system 11. A PT100 thermo meter, monitors the thermal bath, which is kept on temperature by a thermostatic bath (Proline RP 485) element 16.

Results and Discussion

The experimental sorption data are compared with literature data on sorption of CO_2 on shales. It is noted that the data shows a significant decrease in sorption for pressures over 6 MPa, similar to the trend as seen in *Busch et al* (*2008* and *2009*).

It is also noted that negative sorption occurs for pressures > 8 MPa. This can be attributed to the computed void volume from the Helium measurements, versus the void volume of CO_2. A failure in the mass balance computation to determine the sorption potential of the microporous structure of shale was also observed by *Ross et al., 2007* and *Busch et al., 2009*).

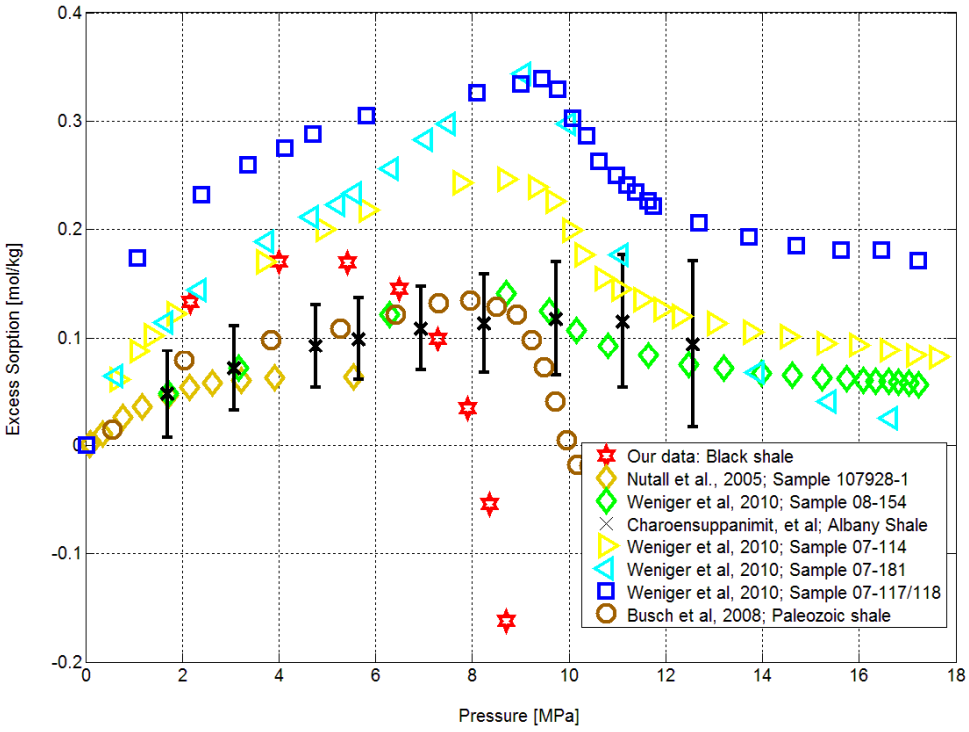

Figure 11:. Measured excess sorption curve versus pressure, Belgian Black shale, versus previous measurements [*Charoensuppanimit et al, Nutall, et al, 2005, Weniger et al, 2010, Busch et all, 2008*].

Compared to other measurements from *Charoensuppanimit et al, Nutall, et al, 2005, Weniger et al, 2010, Busch et al, 2008* as shown in figure 11, a similar curve trend can be recognized, except in those measurements, often higher pressures have been

measured. During future measurements, a larger reference volume will be applied, making it possible to go up to 18 MPa. The Belgium shale shows similar to *Busch et al, 2009*, evidence for the possibility to function besides cap layer also as increased CO_2 reservoir area. When water saturated samples are applied, the CO_2 capacity may even become larger *Busch et al, 2009*. However this also increases the risk of structural failure of the caprock.

3.2.4 Impedance measurement

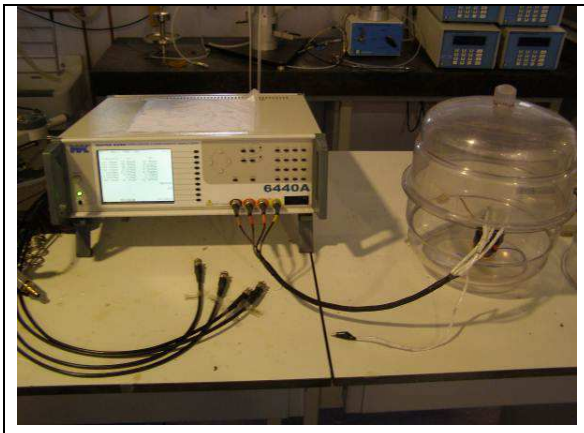

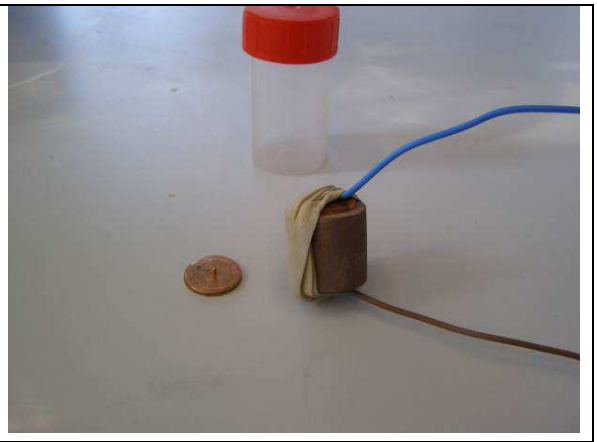

Figure 12 a & b: Wayne Kerr precision component analyser, 6440A and the desiccator in which the sample can be place for CO_2 saturation. Measurements performed at 20.5°C and 50% humidity in the climate lab.

At the start of this project some impedance measurements have been performed under standard atmospheric conditions using a *Wayne Kerr Precision component analyser 6440A*. The equipment is capable of showing the impedance as well as the equivalent resistivity and capacity. Similar to Ohm's law

$$U = ZI \qquad (3.2.3\text{-}1)$$

with *U* the potential difference, *I* the electrical current and *Z* the impedance (a complex value). The equivalent resistivity and capacity are obtained from a parallel resistance (*R*) capacitor (*C*) system.

$$\frac{1}{Z} = \frac{1}{R} + \frac{j\omega C}{1} \qquad (3.2.3\text{-}2)$$

From the capacitor it is possible to obtain the relative permittivity

$$C = \frac{\varepsilon_0 \varepsilon_{rs} A}{h} \qquad (3.2.3\text{-}3)$$

with $\varepsilon_0 = 8.854 \cdot 10^{-12}$ F m^{-1}, A the surface area ($A = 0.25\pi d^2$ with *d=±24.65* mm) and h the height of the sample (*h=±25.75* mm) *[Buijze, 1995; Plug, 2007*].
The tests have been performed on a Mercian mud sample (Figure12b) which was air saturated, N_2 and CO_2 (50%) saturated and CO_2 saturated at atmospheric conditions. This resulted in outcomes as shown in figure 13. The relative permittivity for the three conditions is shown as function of frequency. The qualitative outcome is similar, there is a high permittivity which decreases for higher frequencies. The behaviour for the resistivity is similar.
During a capillary pressure setup, see *figure 1,* it is also capable of measuring the impedance. During the coming months, when time is available, attention will be paid to this possibility [*Buijze, 1995*].

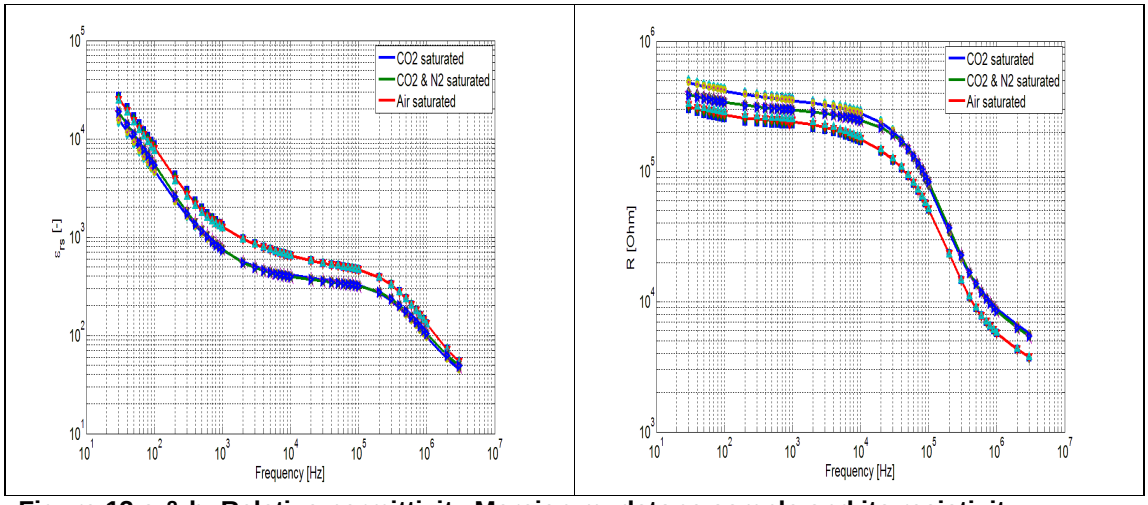

Figure 13 a & b: Relative permittivity Mercian mudstone sample and its resistivity

3.2.5 Shale mechanical properties

3.2.5.1 Equotip measurements

A non-destructive hardness measurement has been performed on the shale with a equotip hardness tester (Figure 14). It functions by applying an impact body, when it hits the surface, to record the velocity, three stages are distinguished. The stage before the impact, where the impact body accelerates. This is followed by the impact, with elasticity/ plasticity effects of the material and the impact body. Finally after the impact, the left over impulse energy is converted into motion of the impact body. Using a magnet and induction coil, a velocity proportional voltage curve is recorded [*Kompatscher, 2004*].

Figure 14: Equo-tip hardness tester

Equo-tip measurements and fracturing experiments on a wide variety of rock types with different characteristics by Verwaal and Mulder (1993) resulted in a logarithmic relationship that converts equo-tip value to unconfined compressive strength (Fig. 15, Verwaal and Mulder, 1993). Figures 16 and 17 show the equo-tip values and converted UCS values respectively for the 5 core sections of well Q4-8 in relation to the position along the cores. Variations in equo-tip hardness can in part be correlated to the sand content in the shale cores. The shale-rich units (red colouration on cores) have on average a lower equo-tip value than the sand-rich layers (more whitish colouration). Depth intervals 2461 m and 2470 m show a clear change in equo-tip value which can exactly be correlated to a change in composition within the cores.

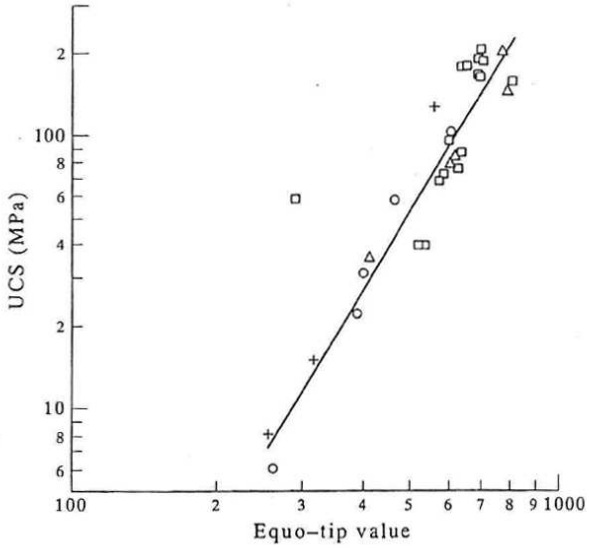

Figure 15: Relation between equo-tip value and unconfined compression strength (UCS) of Verwaal and Mulder (1993). Equotip measurements and unconfined compression testing have been performed on the same samples of a variety of rock types (limestones and sandstones).

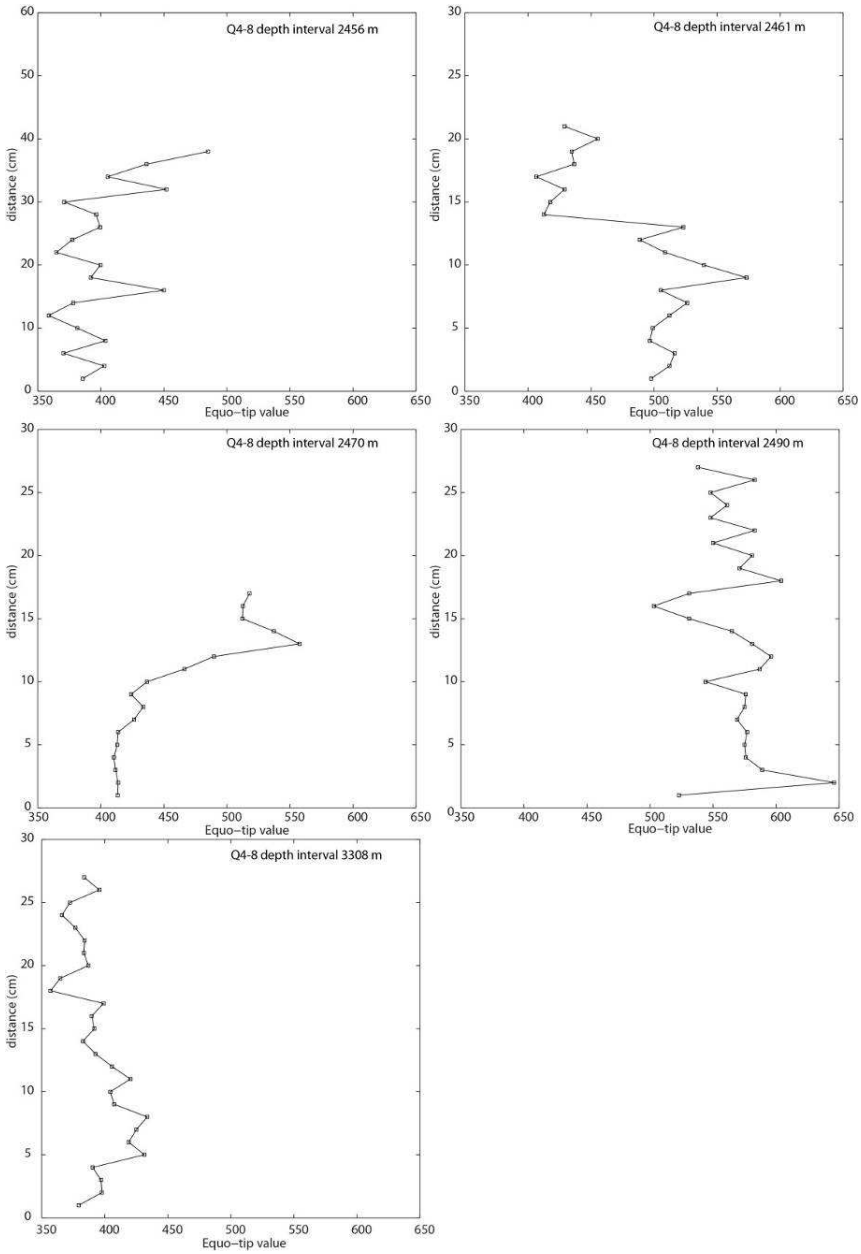

Figure 16: Raw data hardness tests on shales from well Q4-8. Hardness tests have been performed along the long axes of solid cores from depth intervals 2456 m, 2461 m, 2470 m, 2490 m and 3308 m. Measurement intervals have a spacing of 1 or 2 cm.

Depth interval 2456 m	Depth interval 2461 m
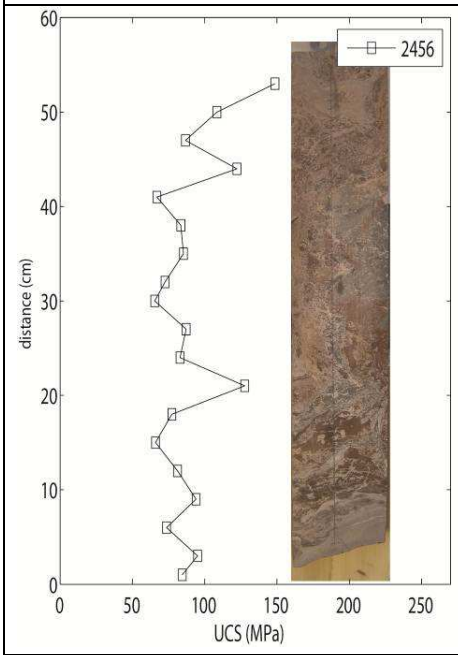	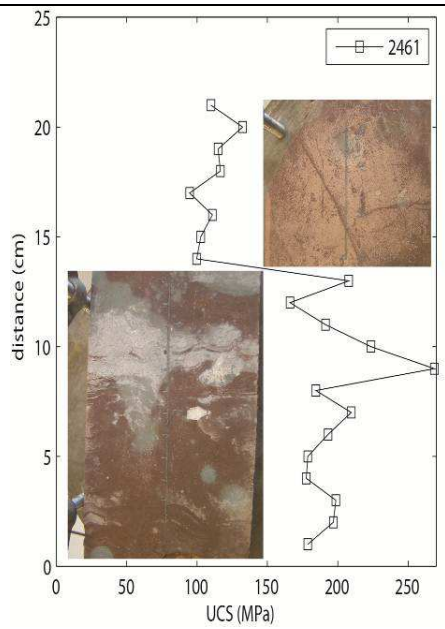

Depth interval 2471 m	Depth interval 2490 m
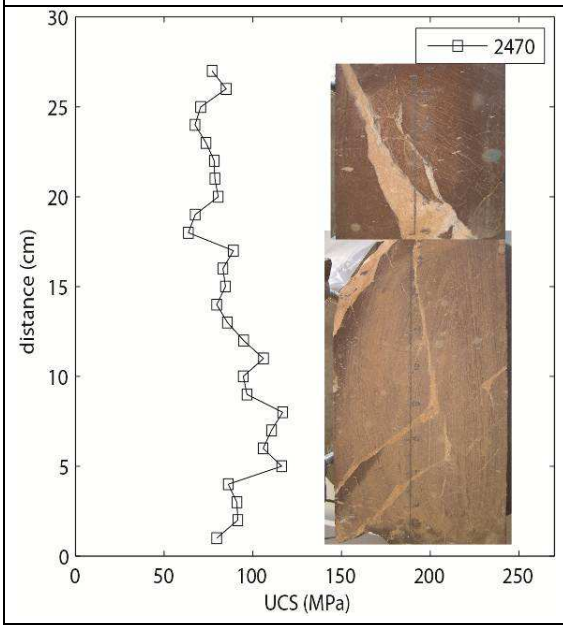	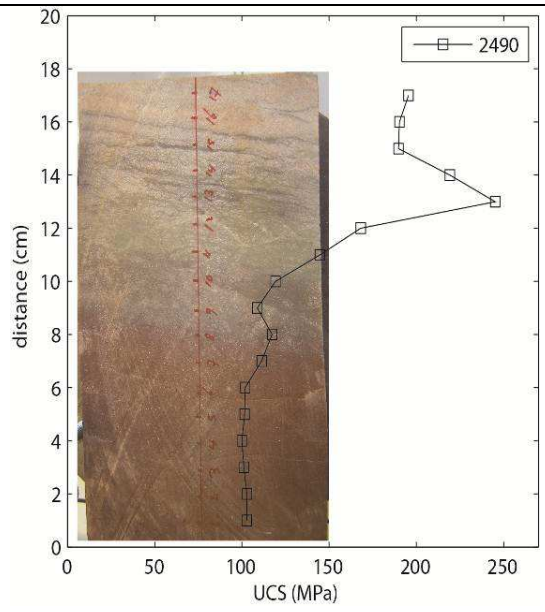

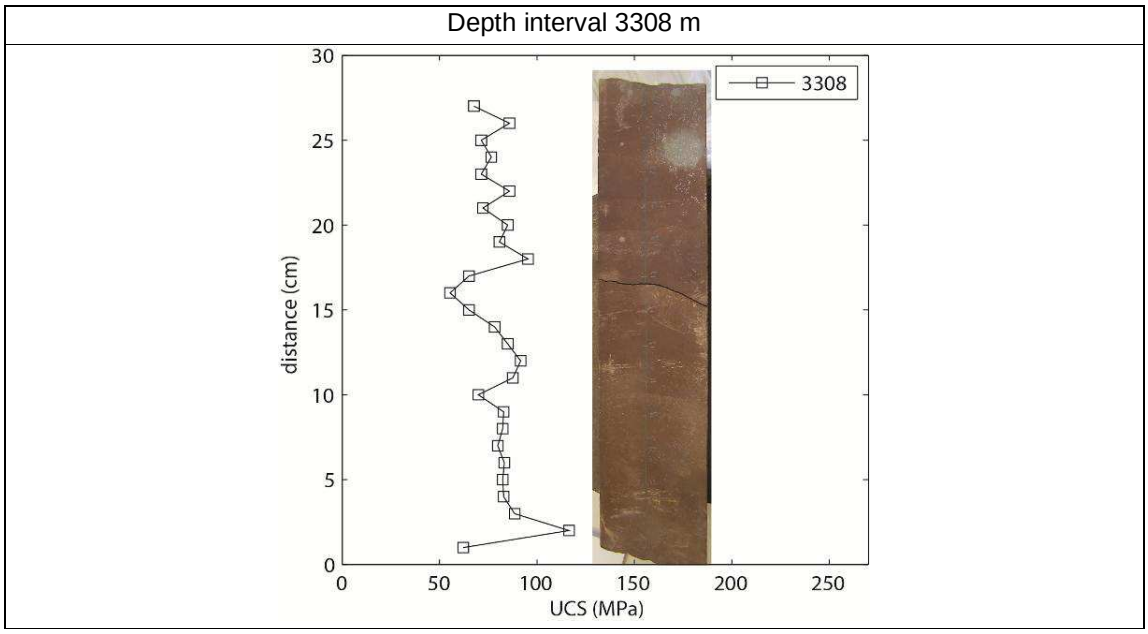

Figure 17: UCS values in MPa of the 5 core sections of well Q4-8. UCS strength values have been calculated from the equo-tip measurements. Relation between the composition and strength is present, particulary visible in the depth intervals 2461 m and 2470 m. Shale-rich units are weaker than sand-rich unit.

3.2.5.2 Unconfined compression experiments on shales from well Q4-8

From the various cores of well Q4-8 four cylindrical samples were drilled with dimensions of 8 cm x 4 cm. Two samples from the depth interval 2456 m contain irregular patches of shale-rich and sand-rich units. No clear layering is observed. The sample from the depth interval of 2461 m is the most shale-rich and shows no presence of sand-rich units. The fourth sample from the depth interval of 2490 m has a sand-rich unit in the bottom 15% of the sample with a clear horizontal layering.

All four samples were tested using uniaxial compressive deformation under unconfined conditions in the Geotechnology Laboratory at TU Delft. Samples were deformed at constant deformation rate and changes of load and vertical and horizontal strain with time were recorded (Figure 18). All samples exhibit a period of linear elastic loading till yield stress conditions after which hardening at slightly lower rates continued till peak stress conditions. Failure and through going fracturing occurred immediately after peak stress conditions for all samples. Small drops in stress before peak stress

conditions are related to the formation of small shear fractures (sample of depth interval 2461 m) without a loss of cohesive strength of the specimen. A through going fracture has then not yet formed. Unconfined compressive strengths of the samples containing both shale-rich and sand-rich intervals are around 100 MPa, whereas the shale only sample has a maximum strength of only 70 MPa. The sand-content in shales thus plays an important role in the strength of shale cap-rocks. Young's modulus E has been determined from the slopes of the stress-strain curves and are around 33-37 GPa for the shale-sand intervals and around 22 GPa for the shale-only interval. This means that more strain can be accommodated in the shale only rocks until failure is reached (Fig. 19).

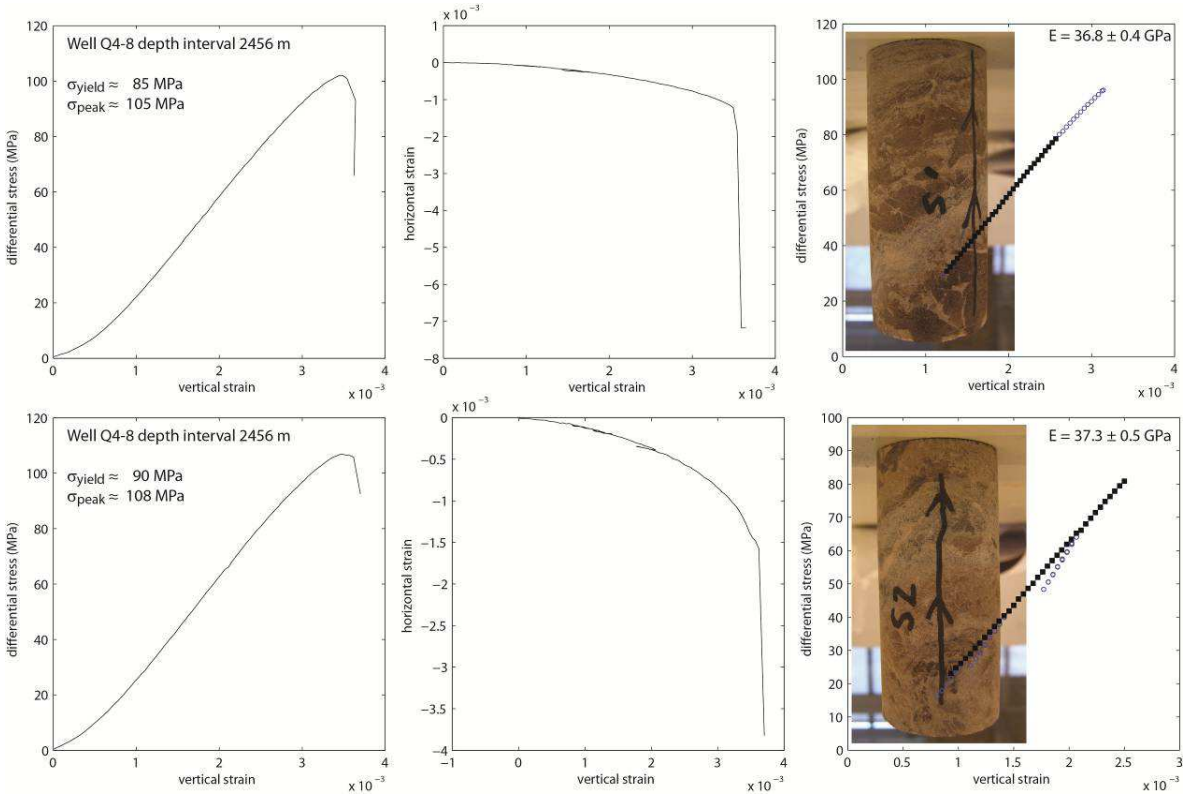

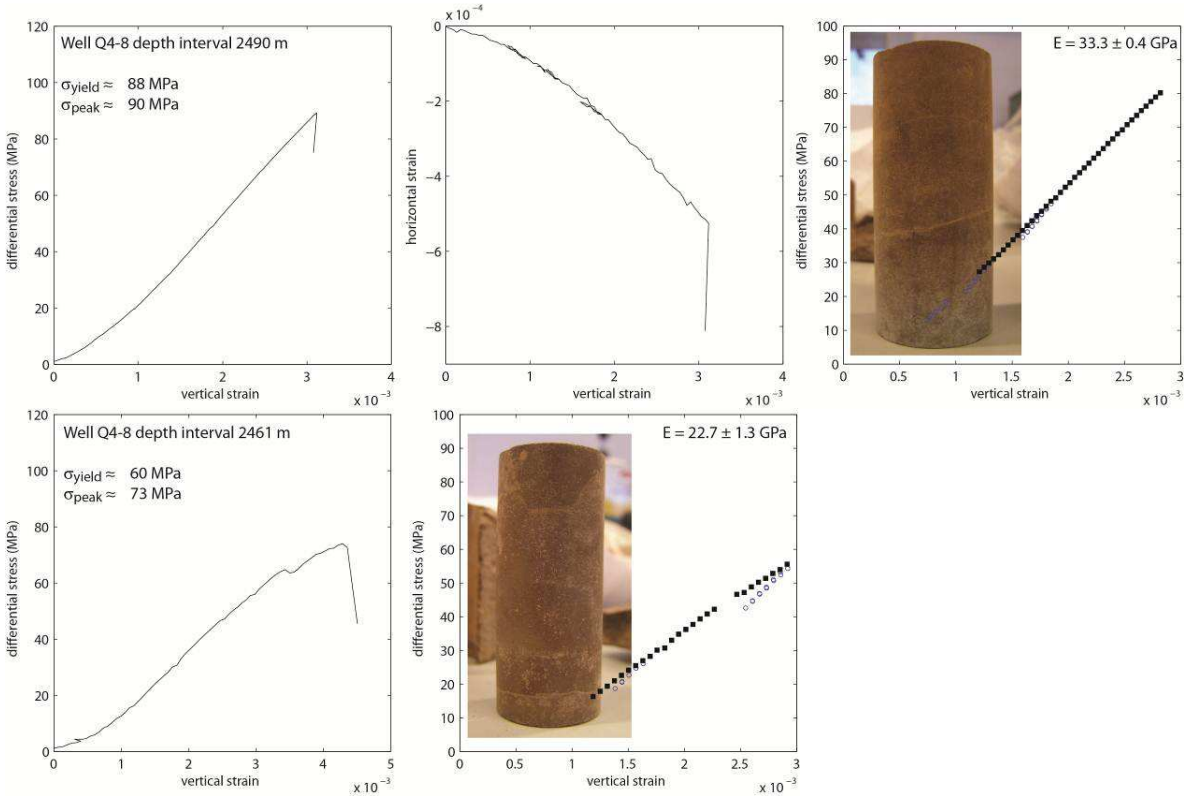

Figure 18:Stress vs. vertical strain curves, vertical strain vs. horizontal strain and stress-strain curves for the linear elastic range for the four samples of shales in well Q4-8 tested in unconfined compression experiments. Yield stress (departure of linear elastic behaviour) and peak strength of each sample is indicated. The Young's modulus is determined from the slope of the stress-strain curves in the linear elastic range.

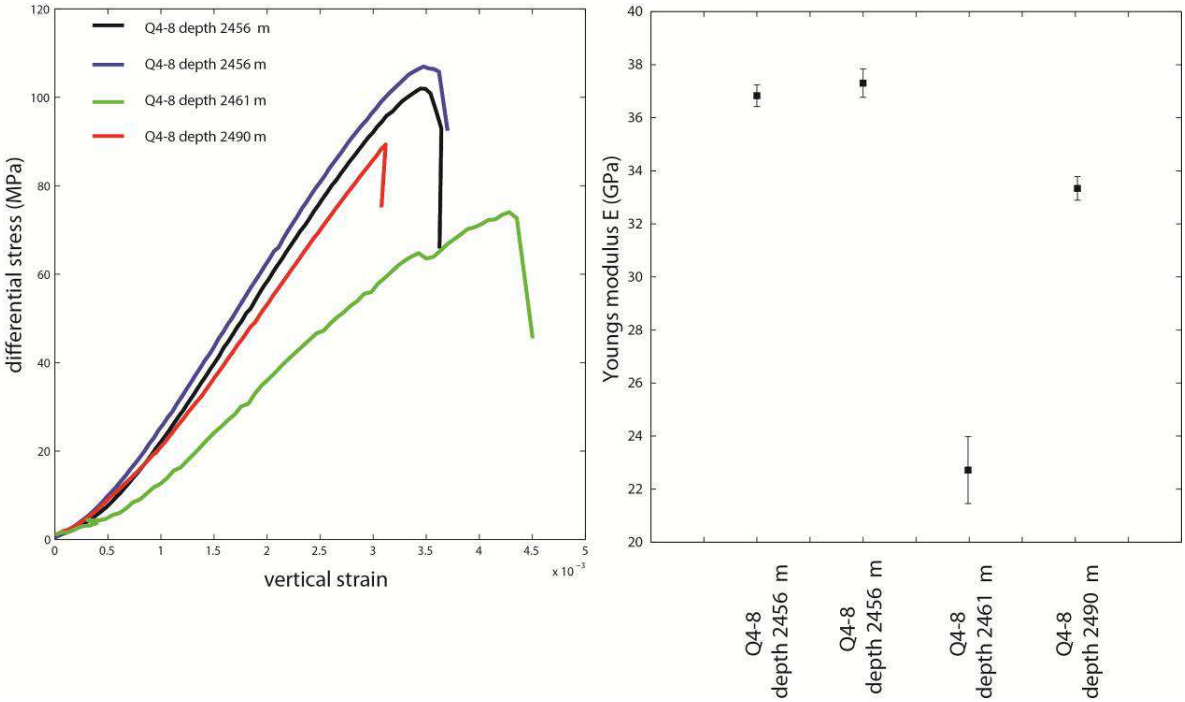

Figure 19: Comparison of the deformation behaviour of the 4 shales from different depth intervals of well Q4-8.

Comparison of the strength data of the shales from well Q4-8 with a series of rock strengths for different materials in Verwaal and Mulder (1993) shows that the shales follow the general trends of the other rock types (Figure 20). The shales are of intermediate strength, stronger than some limestones and sandstones but also weaker than others. This is because porosity has a major control on the unconfined compressive strength of sedimentary rock types. The shales with an estimated porosity around 2.5% follow the general strength-porosity trend in the dataset. The lowest porosity sandstones have a higher strength than the shales of well Q4-8. This explains why the shales with considerable amounts of sand-rich units present have a higher strength than the pure shale interval of 2461 m. It can thus be concluded that both the overall porosity as well as the sand content in shales play an important role in the strength of shale cap-rocks. Because of its low porosities, shales can be considerably stronger than high-porosity sandstones that may be bounding the shales.

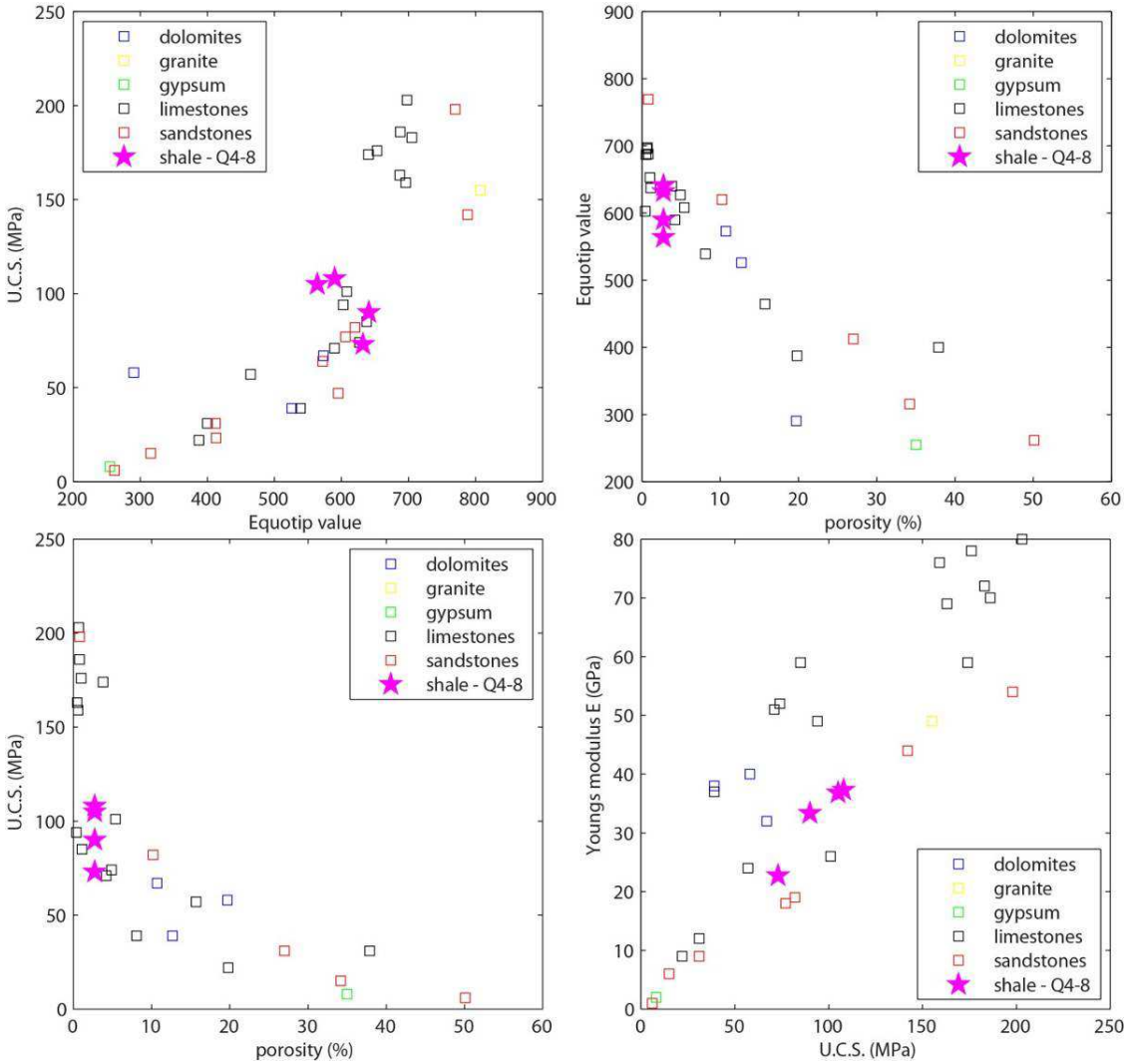

Figure 20: Compilation of unconfined compressive strengths and equo-tip values for various primarily sedimentary rock types. Shales from well Q4-8 follow the porosity-strength trend of sedimentary rocks concluding that both sand-content and porosity play an important role for shale cap rock integrity strengths.

3.2.6 Swelling of the Mercian mud

Mercian mud samples are saturated in demineralised water and water saturated for 10% with NaCl and for 100% saturated with NaCl (Figure 21). The test shows that the Mercian mud sample in demineralised water is most sensitive for swelling and starts to deteriorate immediately. Between the 10% saturated and 100% saturated sample. There

are differences, the 10% starts to deteriorate a bit earlier and more severe, however, over longer time frames, similar effects are observed. This means, that the experiments best can be performed, in case of none-dry samples, with water with salt added (preferably not fully saturated, because of the risk of damaging the applied laboratory setups).

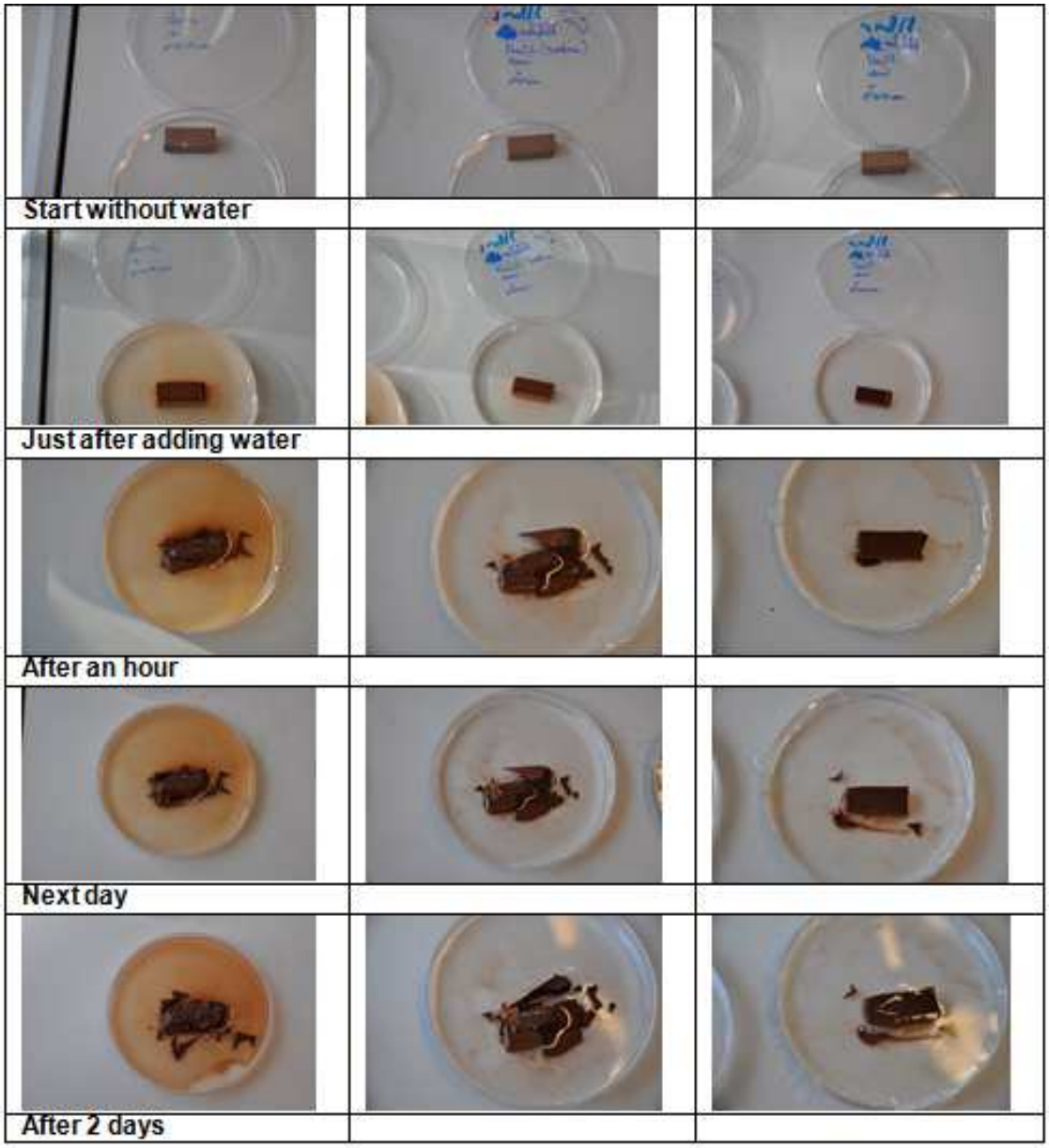

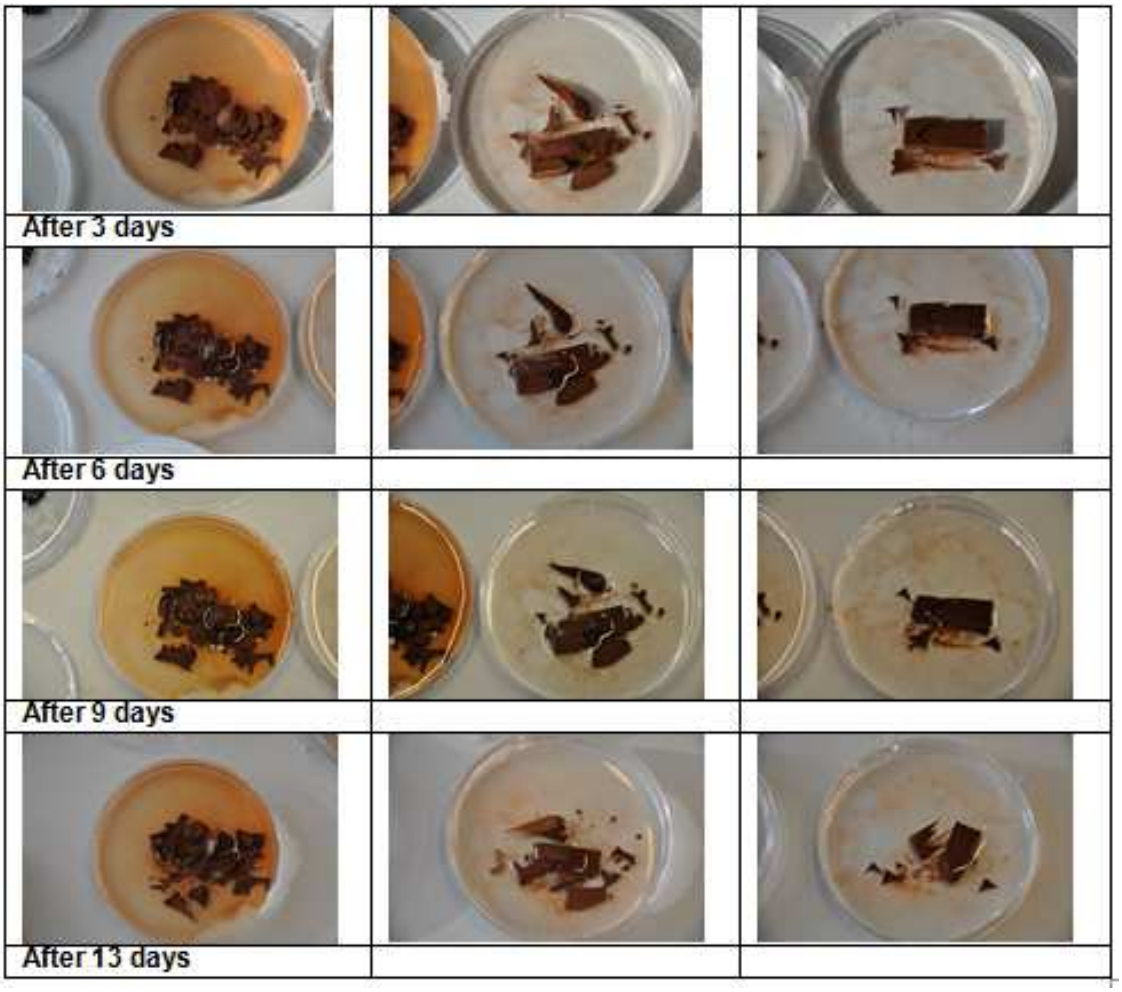

Figure 21: Swelling and disintegration of Mercian in demineralised water (left hand panels), water saturated for 10% with NaCl(middle panels) and for 100% saturated with NaCl (right hand panels). Swelling and disintegration is minimal with fully NaCl saturated mud.

3.2.7 Mud shale permeability

Of all test material, only the Mercian mud porosity (using a pycnometer) has been measured at TU Delft. The Mercian mud permeability is so low that the value has been obtained at Utrecht University. The porosity and permeability of the other samples will be obtained in the near future. The scarcity of the clay material and its difficulty in preparation of homogeneous intact shale samples have slowed the measurements down. Also the XRD and XRF data for Mercian mud and Muschelchalk Röt/ Solling sample has been determined (see appendix).

Type	Location	Porosity	Pemeability	XRD	XRF
		phi	k0		
		[-]	[m2]		
Mercian mud	5	0,14	7E-19	Delft Data	Delft Data
Muschelchalk Röt	2456				
Muschelchalk Röt/ Solling	2461	0,0275	1,5e-19	Delft Data	Delft Data
Solling claystone	2473,4				
Solling claystone	2490				
Dethfurth	3309				

The XRD and XRF data (see appendix) are measured at the 3ME Faculty at Delft University of technology, (by R.W.A. Hendrikx).
The Mercian mud and the Muschelchalk Röt/ Solling sample have been analysed see figure

3.2.7 CT scans of shale samples

Micro CT scans of shales samples show a very homogeneous distribution of phases. Occasional high-density phases (like Fe-oxides or Fe-sulphides) are present within the shale samples but no other heterogeneities occur in the shales analysed (Figure 22). Porosity in the shales is considerably smaller than 1 µm and therefore below the resolution of the micro CT scanner. Porosity measurements of this Mercian mud indicate porosities around 13%, which is thus distributed widely in pores smaller than micrometers in size. CT scans of shales from Q4-8 2461 m show more heterogeneous distribution of phases (clay minerals and sand minerals). Porosities here are lower ~3%) and below the resolution of the CT-scanning technique.

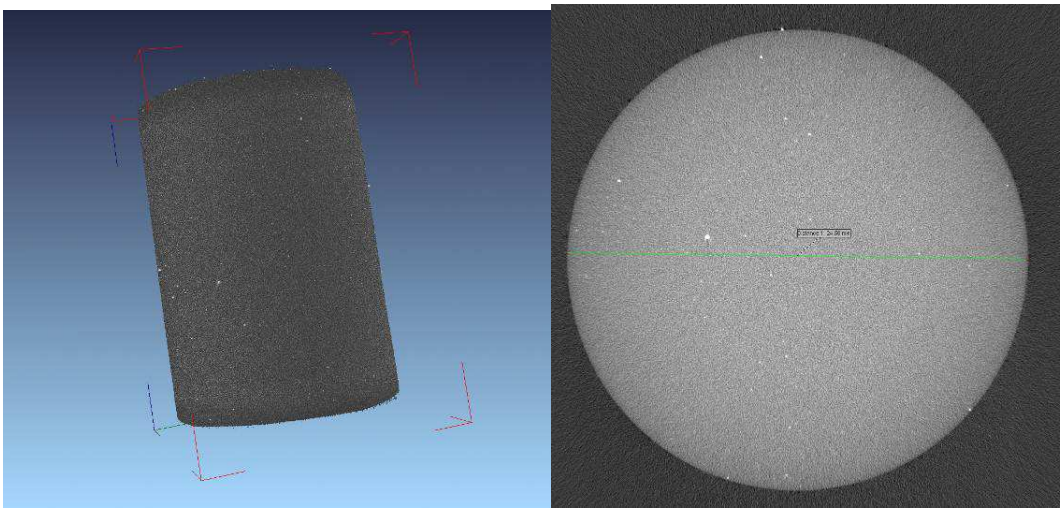

Figure 22: 3D representation of micro CT scan data of Mercian mud and a horizontal slice through the dataset showing the homogeneity of the material. White particles are high density aggregates (most likely Fe-oxides or sulphides).

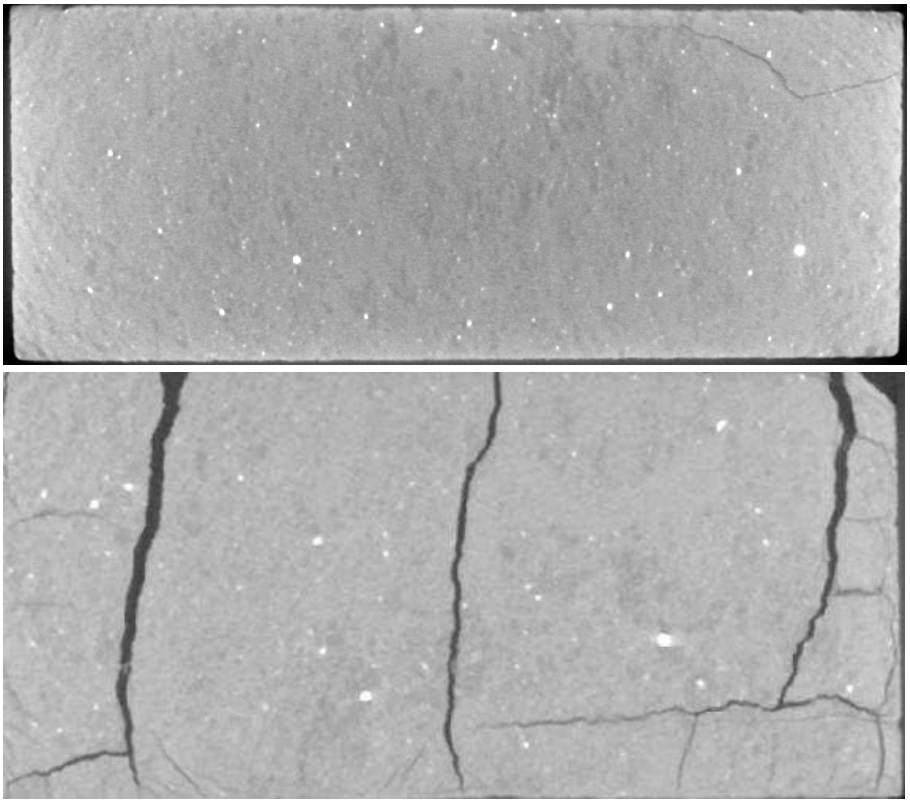

Figure 23: Vertical cross –sections of micro CT dataset of shale sample from well Q4-8 2461 m showing the presence of fractures and heterogeneous distribution of phases

(picture is rotated by 90°: top of sample is the left hand side of the picture). Top panel is shows the shale sample before contact-angle measurements and bottom panel the same sample after the contact angle measurements. Pore sizes are again below the resolution of the micro CT scan.

Because of the limited availability of large samples of consolidated shale from e.g. cores high-pressure CO_2 injection experiments into water-saturated shales inside the CT scanner have not yet been performed. The shale sample that is currently analysed in the capillary pressure set-up will in the near future be analysed in the CT scanner. Then, injection of CO2 from one side of the sample set-up through the Mercian mud and shales will be performed.

3.3 Discussion & conclusions

From the current results, it is concluded that the analysed shales are sensitive for swelling, for this reason tap water is used during the experiments. Increasing the salinity decreases the swelling, however for high salt saturations, the experimental setups can potentially be damaged. Swelling increases the risk of fracturing. For a more detailed analyses of this problem, originally saturated clay samples are necessary, which are not dried before we can analyse them in the laboratory.

The wetting behaviour, contact angle and capillary pressure, are important for the integrity of the rocks. The used Muschelchalk Rot/ Solling sample showed the sample stayed water-wet upto 120 bars. And following the trend will become intermediate wet at much higher pressures. The capillary measurements show that the capillary pressure is lower than those for coal and sand, but have similar trends.

From the experiments it is noted that the modified manometric sorption apparatus is capable of determining the sorption of CO_2 on shales. In addition, the rate of sorption can be determined, which for Belgian Black shales is of the order of tens of hours (*Khosrokhavar et al, 2012*).

From the mechanical stress tests it can be concluded that the sand-content in shales plays an important role in the strength of shale cap-rocks. Pure shale has a considerable lower maximum strength. The overall porosity as well as the sand content in shales play an important role in the strength of shale cap-rocks. Because of its low porosities, shales can be considerably stronger than high-porosity sandstones that may be bounding the shales.

During future experiments we will broaden our view by analysing the wetting behaviour (capillary pressure and contact angle) of more shale samples.

4 References

Al-Garni, M.T., Al-Anazi, B.D. (2008). Investigation of wettability effects on capillary pressure, and irreducible saturation for Saudi crude oils, using rock centrifuge . Oil and Gas Business.

Berendsen, H.J.A (2011). De vorming van het land: inleiding in de geologie en de geomorfologie, van Gorcum van Comp. B.V., The Netherlands

Buijze, W. and Roest, R. (1995). Inleiding Elektriciteit en Magnetisme. Delft University Press, The Netherlands.

Busch, A., Alles, S., Gensterblum, Y., Prinz, D., Dewhurst, D., Raven, M.D., Stanjek, H., Krooss, M.B., (2008). Carbon dioxide storage potential of shales, Internationl journal of greenhouse gas control, 2, 2008, 297-308.

Busch, A., Alles, S., Krooss, M.B. Stanjek, H. Dewhurst, D., (2009), Effects of physical sorption and chemical reactions of CO2 in shaly caprocks, Energy Procedia, 1, 3229--3235

Charoensuppanimit, P., Mohammed, S., Robinson, Jr. R., Gasem, K.A.M., High-Pressure Adsorption of Gases on (Albany) Shales: Measurements and Modeling, AIChE, 2011 & Journal of Coal Geology, 2012

Chiquet, P., Broseta, D., U of Pau and S. Thibeau (2005). Capillary alteration of shaly caprocks by carbon dioxide. SPE/ EUROPEC 94183-MS.

Hemert, P. van (2010). Preliminary data on entry pressure, wetting behaviour, and transport properties of coal/caprocks from the DSM site, CATO2, The Netherlands

Hemert, P. van (2009). Manometric determination of supercritical gas sorption in coal . PhD thesis, Delft University of Technology, Delft, The Netherlands.

Khosrokhavar R., Schoemaker, C., Battistutt, E., Wolf K.H., Bruining, H., Sorption of CO_2 in Shales Using the Manometric Set-up*, SPE-EUROPEC, 2012*

Kompatscher, M., (2004). Equotip – Rebound hardness testing after D. Leeb, Hardness Measurements Theory and Application in Laboratories and Industries, 1--7.

Nutall, B.C., Eble,, C.F., Drahovzal, J.A., Bustin, M., (2005), Analysis of Devonian Black shales in Kentucky for poretntial carbon dioxide sequestration and enhanced natural gas production, Kentucky Geological Survey, Unversity of Kentucky, Lexington, Kentucky.

Plug, W.-J., Mazumder, S., Bruining, J., Siemons, N., Wolf, K.H., (2006). Capillary pressure and Wettability of the coal-water-carbon dioxide system at high pressures, Coalbed methanse symposium 2006, 606, 1--15.

Plug, W.-J. (2007). Measurements of capillary pressure and electric permittivity of gas-water systems in porous media at elevated pressures; application to geological storage of CO_2 in aquifers and wetting behaviour in coal, PhD thesis, Delft University of Technology, Delft, The Netherlands.
Plug, W.-J., Bruining, J. (2007), Capillary pressure for the sand–CO2–water system under
various pressure conditions. Application to CO2 sequestration, Advances in water resources, 2339--2353

Ross, D.J.K., Bustin, R.M., (2007), Impact of mass balance calculations on adsorption capacities
in microporous shale gas reservoirs, Fuel, 86, 2696—2706.

Seleznev, N.V. (2005). Theoretical and laboratory investigation of dielectric properties of partially saturated carbonate rocks, PhD thesis, Delft University of Technology, Delft, The Netherlands.

Shakhashiri, B.Z. (2008).Chemical of the week, Carbon Dioxide, CO_2, General chemistry, www.scifun.org.

Siemons, N., Bruining, H. ,Wolf, K.H., Plug, W.-J (2006). Pressure dependenceof the CO2 contact angle on bituminous coal and semi – anthracite in water, Coalbed methanse symposium 2006, 605, 1--12.

Siemons, N. (2007). Carbon dioxide transport and retention in coal. PhD thesis, Delft University of Technology, Delft, The Netherlands.

Verwaal, W., Mulder, A., 1993. Technical note: Estimating rock strength with the equotip hardness tester. International Journal of Rock Mechanics Mineral Science and Geomechanics Abstracts 39, 659-662.

Weniger, P. Kalkreuth, W., Busch, A., Krooss, B.M., (2010). High-pressure methane and carbon sorption on coal and shale samples from the Parana Basin, Brazil, International Journal of Coal Geology 84, 190-205.

CATO2, WP3.3, (2010), http://www.co2-cato.org/cato-2/themes/sp3-underground-storage-monitoring-and-verification/33-cap-rock-and-fault-integrity

TNO National Geological Survey (2004).Geological Atlas of the subsurface of the Netherlands - onshore,TNO, The Netherlands

5 Appendix

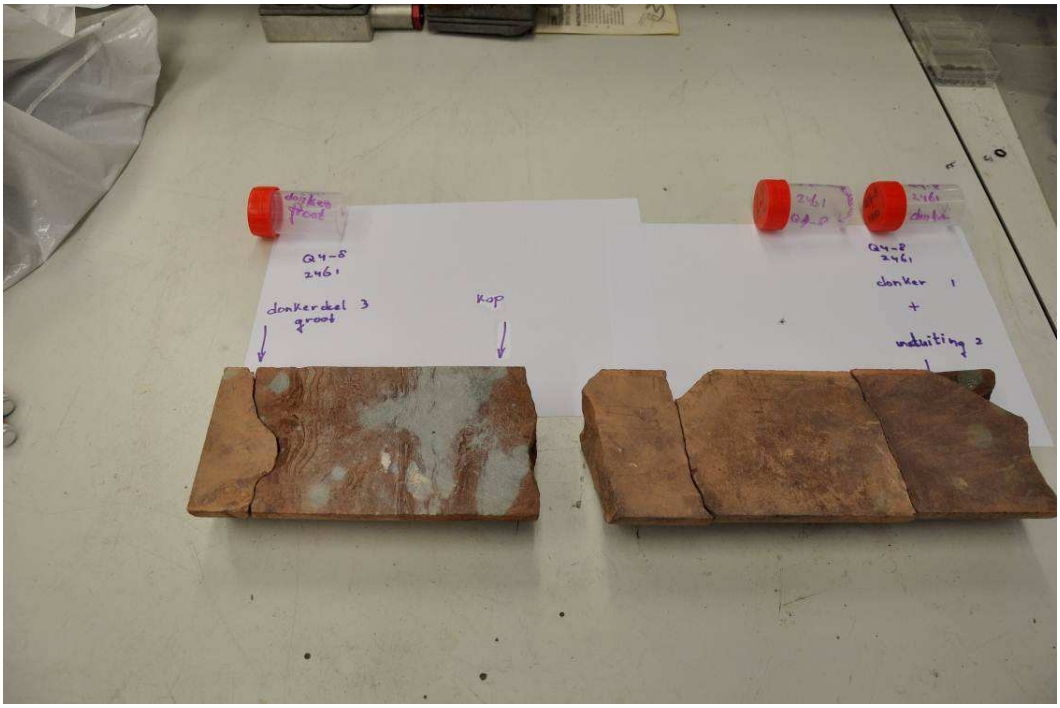

Figure 24: Muschelchalk Röt/ Solling several sample positions

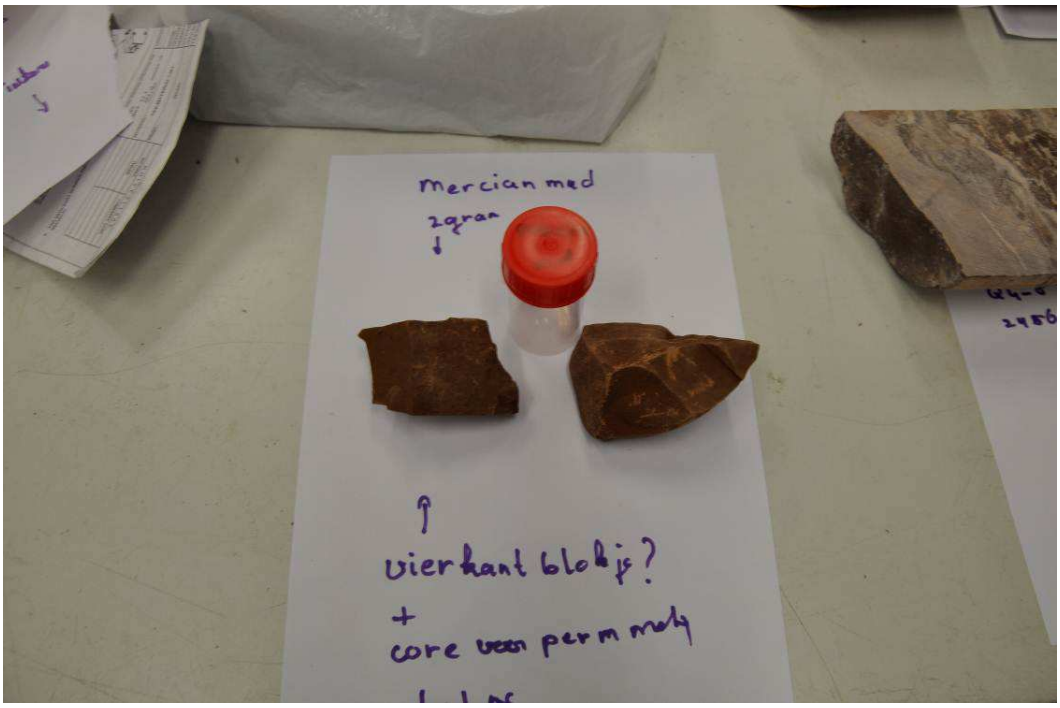

Figure 25: Mercian mud sample

Figure 26: Muschelchalk Röt/ Solling, sample 1

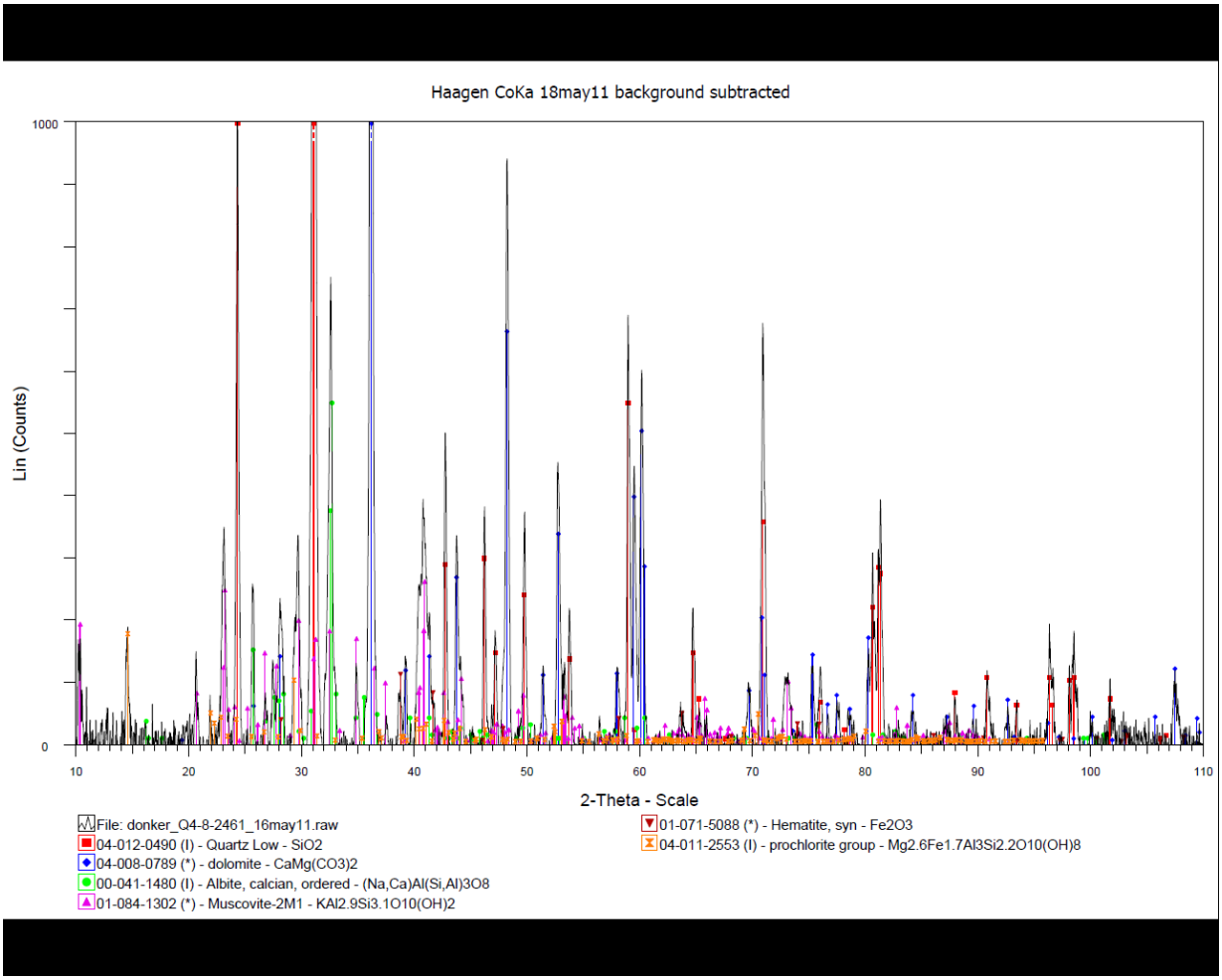

Table Computed minerals, without organic matter sample 2

	Mole [%]	Weight [%]	Volume [%]
Musovite	0.078	0.269	0.268
Kalinite	0.019	0.043	0.047
Chlorite	0.004	0.018	0.018
Dolomite	0.299	0.240	0.237
Quartz	0.494	0.259	0.276
Pure Albite	0.040	0.091	0.097
Haemettite	0.033	0.045	0.024
Anhydrite	0.018	0.021	0.020
Rutile	0.009	0.006	0.004
Ca-Apatite	0.001	0.004	0.003
Halite	0.007	0.004	0.005
Total	**1.000**	**1.000**	**1.000**

Figure 27: Muschelchalk Röt/ Solling, sample 2

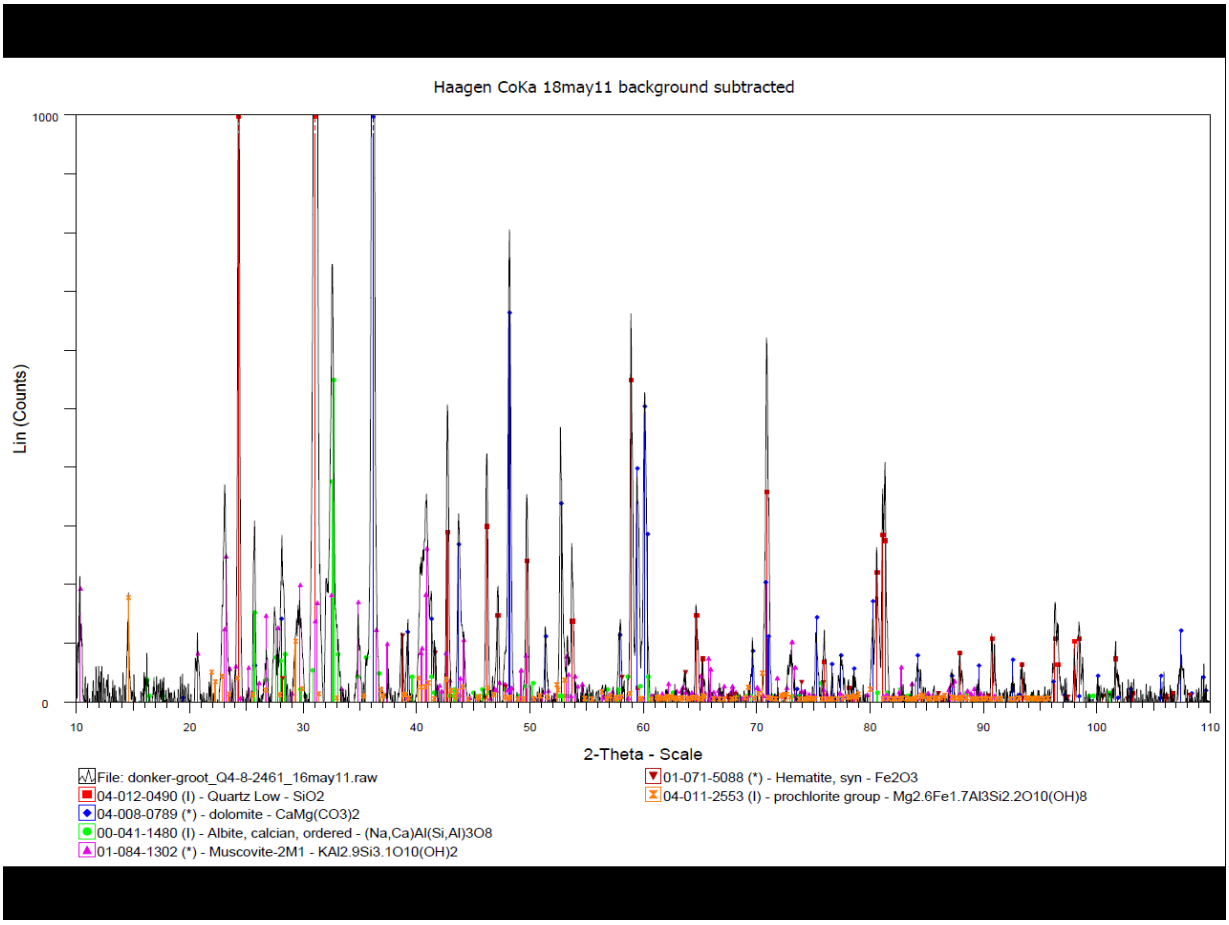

Table Computed minerals, without organic matter sample 2

	Mole [%]	Weight [%]	Volume [%]
Musovite	0.076	0.266	0.265
Kalinite	0.017	0.039	0.043
Chlorite	0.002	0.012	0.011
Dolomite	0.294	0.240	0.235
Quartz	0.508	0.269	0.286
Pure Albite	0.047	0.108	0.116
Haemettite	0.033	0.046	0.025
Anhydrite	0.003	0.004	0.004
Rutile	0.009	0.006	0.004
Ca-Apatite	0.001	0.004	0.003
Halite	0.010	0.005	0.007

Total	**1.000**	**1.000**	**1.000**

Figure 28: Muschelchalk Röt/ Solling, sample 3

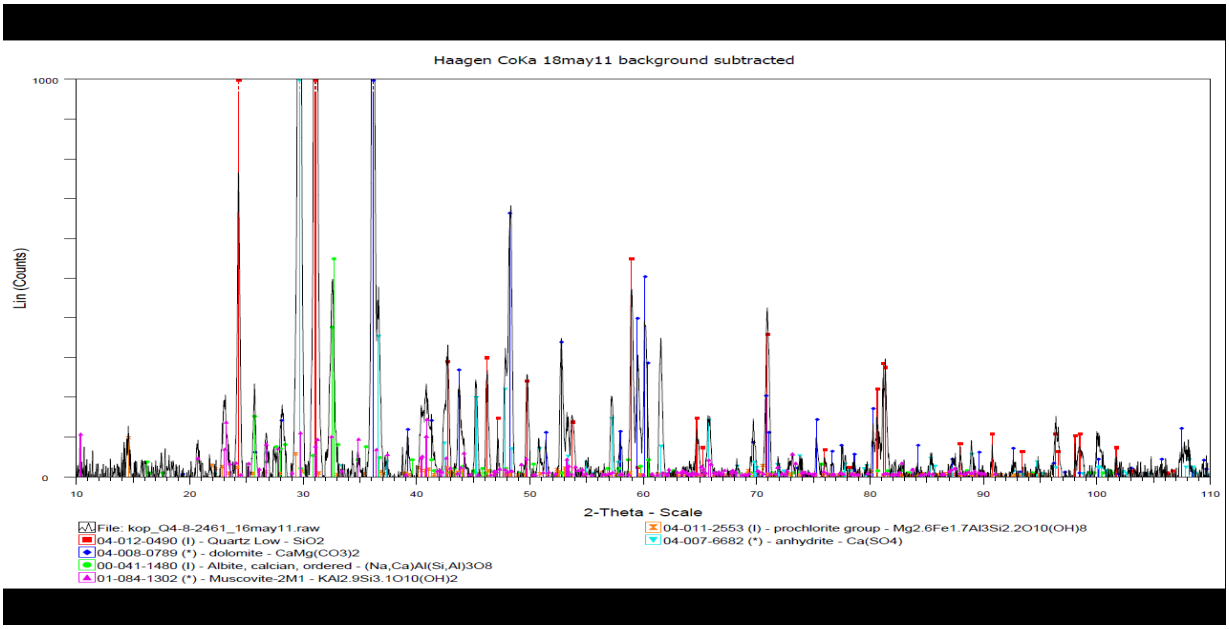

Table Computed minerals, without organic matter sample 3

	Mole [%]	Weight [%]	Volume [%]
Muscovite	0.069	0.210	0.211
Chlorite	0.024	0.107	0.106
Dolomite	0.144	0.102	0.101
Quartz	0.435	0.200	0.215
ure Albite	0.043	0.087	0.094
Haemettite	0.015	0.019	0.010
Anhydrite	0.253	0.264	0.253
Rutile	0.009	0.005	0.004
Ca-Apatite	0.001	0.003	0.003
Halite	0.007	0.003	0.004
Total	**1.000**	**1.000**	**1.000**

Table Computed minerals, with organic matter sample 3

	Mole [%]	Weight [%]	Volume [%]
Muscovite	0.044	0.198	0.187
Chlorite	0.015	0.101	0.094
Dolomite	0.092	0.096	0.089
Quartz	0.277	0.189	0.191
Pure Albite	0.028	0.082	0.083
Haemettite	0.010	0.018	0.009

Anhydrite	0.161	0.249	0.224
Rutile	0.006	0.005	0.003
Ca-Apatite	0.000	0.003	0.002
Halite	0.005	0.003	0.004
Organic matter	0.364	0.057	0.113
Total	**1.000**	**1.000**	**1.000**

Figure 29: Mercian mud, sample

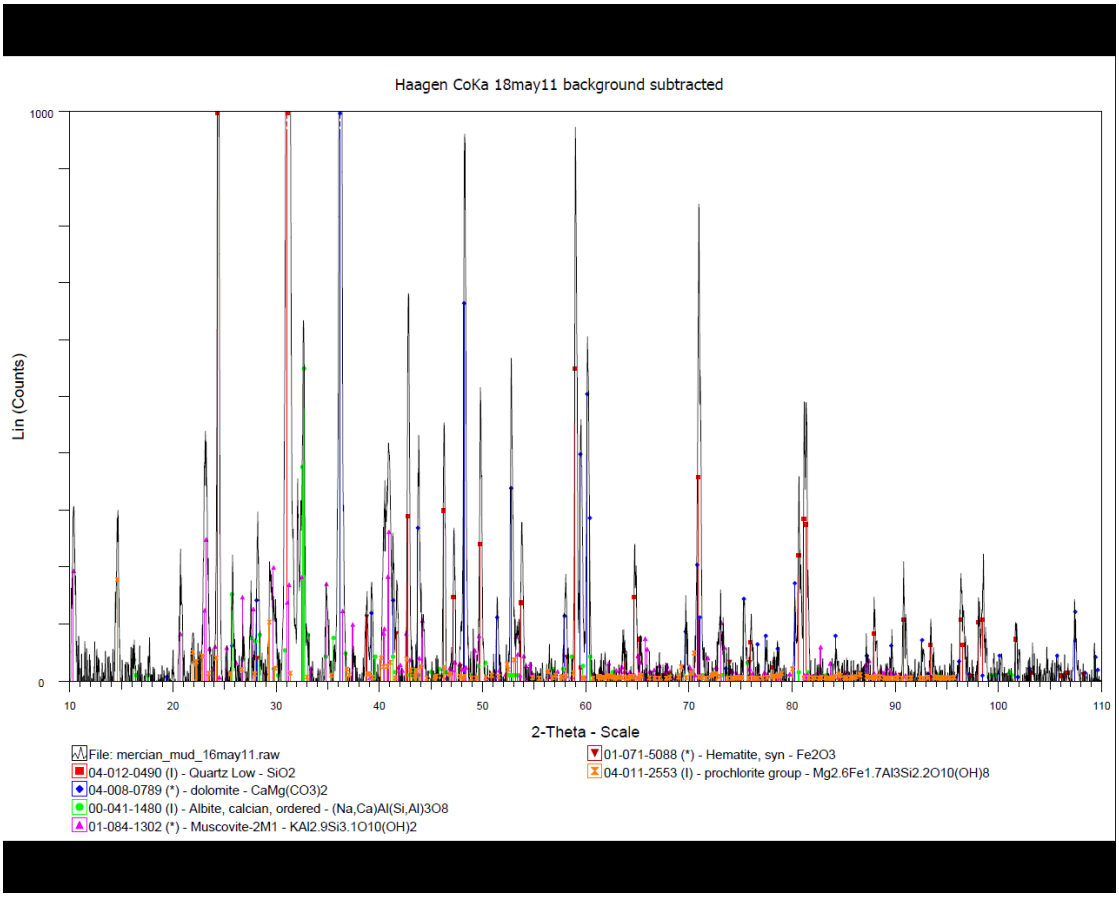

Table Computed minerals, without organic matter Mercian mud

	Mole [%]	*Weight [%]*	*Volume [%]*
Musovite	0.080	0.273	0.272
Kaolinite	0.032	0.071	0.078
Chlorite	0.011	0.053	0.052
Dolomite	0.273	0.215	0.212
Quartz	0.529	0.271	0.289
Pure Albite	0.025	0.056	0.060
Haemettite	0.035	0.048	0.026

Anhydrite	0.002	0.002	0.002
Rutile	0.009	0.006	0.004
Ca-Apatite	0.001	0.003	0.003
Halite	0.002	0.001	0.001
Total	**1.000**	**1.000**	**1.000**

Figure 30: Black shale

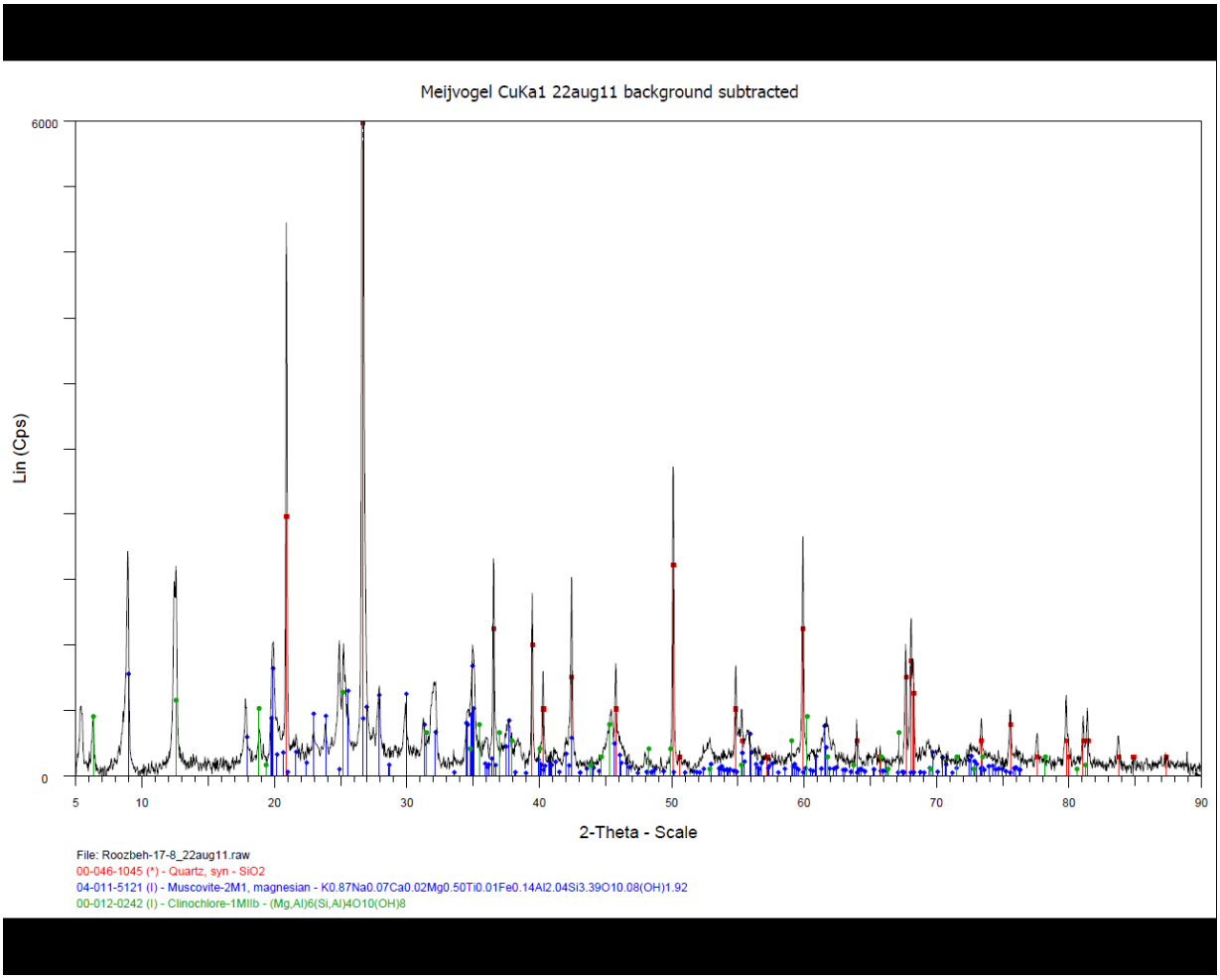

Sample 1, Muschelchalk Röt/ Solling at 2460

m	m/m%	StdErr	m	m/m%	StdErr	m	m/m%	StdErr
SumBe..F	0.140	0.029	29+CuO	<		52 TeO2	<	
11+Na2O	1.35	0.13	30+ZnO	0.0144	0.0009	53 I	<	
12+MgO	6.05	0.27	31+Ga2O3	<		55 Cs2O	<2e	0.0045
13+Al2O3	14.78	0.24	32 GeO2	<		56+BaO	0.0814	0.0071
14+SiO2	48.15	0.64	33 As2O3	<		SumLa..Lu	0.005	0.048
15+P2O5	0.152	0.003	34 SeO2	<		72 HfO2	<	
15 P			35 Br	<		73 Ta2O5	<	
16+SO3	1.23	0.12	37+Rb2O	0.0135	0.0007	74 WO3	<	
16 S			38+SrO	0.0269	0.0030	75 Re2O7	<	
17+Cl	0.228	0.025	39+Y2O3	<		76 OsO4	<	
18+Ar	0.0105	0.0019	40+ZrO2	0.0283	0.0014	77 IrO2	<	
19+K2O	3.16	0.20	41 Nb2O5	<		78 PtO2	<	
20+CaO	8.22	0.32	42+MoO3	<		79 Au	<	
21 Sc2O3	<		44+RuO2	<		80 HgO	<	
22+TiO2	0.587	0.065	45+Rh2O3	<		81 Tl2O3	<	
23+V2O5	0.0145	0.0013	46 PdO	<		82 PbO	<	
24+Cr2O3	0.0140	0.0016	47 Ag2O	<		83 Bi2O3	<	
25+MnO	0.109	0.005	48 CdO	<		90 ThO2	<	
26+Fe2O3	4.63	0.25	49 In2O3	<		92 U3O8	<	
27 Co3O4	<		50 SnO2	<		94 PuO2	<	
28+NiO	<		51 Sb2O3	<		95 Am2O3	<	

==== Light Elements =====			==== Noble Elements =====			=== Lanthanides ====	
SumBe.. F	0.140	0.029	44+RuO2	<		57 La2O3	<
4 BeO	<		45+Rh2O3	<		58 CeO2	<
5 B2O3	<		46 PdO	<		59 Pr6O11	<
6 CO2	<		47 Ag2O	<		60 Nd2O3	<
7 N	<		75 Re2O7	<		62+Sm2O3	<
8 O	<		76 OsO4	<		63 Eu2O3	<
9+F	0.140	0.029	77 IrO2	<		64 Gd2O3	<
			78 PtO2	<		65+Tb4O7	<
			79 Au	<		66 Dy2O3	<
						67 Ho2O3	<
						68+Er2O3	<
						69 Tm2O3	<

						70 Yb2O3	**<**
						71 Lu2O3	**<**

Sample 2, Muschelchalk Röt/ Solling at 2460

m	m/m%	StdErr	m	m/m%	StdErr	m	m/m%	StdErr
SumBe..F	**0.188**	**0.030**	**29 CuO**	**<**		**52 TeO2**	**<**	
11+Na2O	**0.777**	**0.086**	**30+ZnO**	**0.0052**	**0.0008**	**53 I**	**<**	
12+MgO	**6.58**	**0.28**	**31+Ga2O3**	**<**		**55 Cs2O**	**<**	
3+Al2O3	**16.39**	**0.25**	**32 GeO2**	**<**		**56+BaO**	0.0413	**0.0075**
14+SiO2	**50.98**	**0.63**	**33 As2O3**	**<**		**sumLa..Lu**	**0.012**	**0.052**
15+P2O5	**0.141**	**0.003**	**34 SeO2**	**<**		**72 HfO2**	**<**	
15 P			**35 Br**	**<**		**73 Ta2O5**	**<**	
16+SO3	**0.149**	**0.017**	**37+Rb2O**	**0.0121**	**0.0006**	**74 WO3**	**<**	
16 S			**38+SrO**	**0.0157**	**0.0017**	**75 Re2O7**	**<**	
17+Cl	**0.0692**	**0.0077**	**39+Y2O3**	**<**		**76 OsO4**	**<**	
18+Ar	**0.0064**	**0.0019**	**40+ZrO2**	**0.0329**	**0.0016**	**77 IrO2**	**<**	
19+K2O	**3.33**	**0.20**	**41 Nb2O5**	**<**		**78 PtO2**	**<**	
20+CaO	**6.98**	**0.29**	**42+MoO3**	**<**		**79 Au**	**<**	
21 Sc2O3	**<**		**44+RuO2**	**<**		**80 HgO**	**<**	
22+TiO2	**0.643**	**0.071**	**5+Rh2O3**	**<**		**81 Tl2O3**	**<**	
23+V2O5	**0.0152**	**0.0013**	**46+PdO**	**<**		**82 PbO**	**<**	
24+Cr2O3	**0.0165**	**0.0018**	**47 Ag2O**	**<**		**83 Bi2O3**	**<**	
5+MnO	**0.0876**	**0.0044**	**48 CdO**	**<**		**90 ThO2**	**<**	
6+Fe2O3	**5.57**	**0.27**	**49 In2O3**	**<**		**92 U3O8**	**<**	
27 Co3O4	**<**		**50 SnO2**	**<**		**94 PuO2**	**<**	
28+NiO	**<**		**51 Sb2O3**	**<**		**95 Am2O3**	**<**	

==== Light Elements =====			**==== Noble Elements =====**			**===**	**Lanthanides**	**====**
SumBe..F	0,188	0,03	44+RuO2	<		57+La2O3	0,0056	0,0014
4 BeO			45+Rh2O3	<		58 CeO2	<	
5 B2O3			46+PdO	<		59 Pr6O11	<	

6 CO2			47 Ag2O	<		60 Nd2O3	<	
7 N			75 Re2O7	<		62+Sm2O3	<	
8 O			76 OsO4	<		63 Eu2O3	<	
9+F	0,188	0,03	77 IrO2	<		64 Gd2O3	<	
			78 PtO2	<		65+Tb4O7	<	
			79 Au	<		66 Dy2O3	< <	
						67 Ho2O3		
						68+Er2O3	<	
						69 Tm2O3	<	
						70 Yb2O3	<	
						71 Lu2O3	<	

Sample 3, Muschelchalk Röt/ Solling at 2460

m	m/m%	StdErr	m	m/m%	StdErr	m	m/m%	StdErr
SumBe..F	**0.189**	**0.035**	**29+CuO**	<		**52 TeO2**	<	
11+Na2O	**1.26**	**0.12**	**30+ZnO**	**0.0074**	**0.0009**	**53 I**	<	
12+MgO	**5.40**	**0.25**	**31+Ga2O3**	<		**55 Cs2O**	<	
13+Al2O3	**12.09**	**0.22**	**32 GeO2**	<		**56+BaO**	**0.0666**	**0.0069**
14+SiO2	**40.60**	**0.62**	**33 As2O3**	<		**SumLa..Lu**	**0.009**	**0.050**
15+P2O5	**0.127**	**0.003**	**34 SeO2**	<		**72 HfO2**	<	
15 P	<		**35 Br**	<		**73 Ta2O5**	<	
16+SO3	**16.47**	**0.43**	**37+Rb2O**	**0.0113**	**0.0006**	**74 WO3**	<	
16 S	<		**38+SrO**	**0.0675**	**0.0075**	**75 Re2O7**	<	
17+Cl	**0.202**	**0.022**	**39+Y2O3**	<		**76 OsO4**	<	
18+Ar	**0.0129**	**0.0021**	**40+ZrO2**	**0.0258**	**0.0013**	**77 IrO2**	<	
19+K2O	**2.59**	**0.18**	**41 Nb2O5**	<		**78 PtO2**	<	
20+CaO	**14.69**	**0.42**	**42+MoO3**	<		**79 Au**	<	
21 Sc2O3	<		**44+RuO2**	<		**80 HgO**	<	
22+TiO2	**0.557**	**0.062**		<		**81 Tl2O3**	<	

			45+Rh2O3					
23+V2O5	0.0173	0.0015	46 PdO	<		82 PbO	<	
24+Cr2O3	0.0160	0.0018	47 Ag2O	<		83 Bi2O3	<	
25+MnO	0.103	0.005	48 CdO	<		90 ThO2	<	
26+Fe2O3	3.47	0.21	49 In2O3	<		92 U3O8	<	
27+Co3O4	<		50 SnO2	<		94 PuO2		
28 NiO	<		51 Sb2O3	<		95 Am2O3		

==== Light Elements =====			==== Noble Elements =====		=== Lanthanides ====	
SumBe..F	0.189	0.035	44+RuO2	<	57+La2O3	<
4 BeO			45+Rh2O3	<	58 CeO2	<
5 B2O3			46 PdO	<	59 Pr6O11	<
6 CO2			47 Ag2O	<	60 Nd2O3	<
7 N			75 Re2O7	<	62 Sm2O3	<
8 O			76 OsO4	<	63 Eu2O3	<
9+F	0.189	0.035	77 IrO2	<	64 Gd2O3	<
			78 PtO2	<	65+Tb4O7	<
			79 Au	<	66 Dy2O3	<
					67 Ho2O3	<
					68+Er2O3	<
					69 Tm2O3	<
					70 Yb2O3	<
					71 Lu2O3	<

Mercian mud

m	m/m%	StdErr	m	m/m%	StdErr	m	m/m%	StdErr
SumBe..F	0.192	0.031	29 CuO	<		52 TeO2	<	
11+Na2O	0,821	0,091	30+ZnO	0,0059	0,0009	53 I	<	
12+MgO	6,99	0,28	31+Ga2O3	<		55 Cs2O	<	
13+Al2O3	17,54	0,25	32 GeO2	<		56+BaO	0,0436	0,0082
14+SiO2	55,24	0,55	33 As2O3	<			0,013	0,059

						SumLa..Lu		
15+P2O5	0,156	0,003	34 SeO2	<		72 HfO2	<	
15 P	<		35 Br	<		73 Ta2O5	<	
16+SO3	0,165	0,018	37+Rb2O	0,0139	0,0007	74 WO3	<	
16 S	<		38+SrO	0,018	0,002	75 Re2O7	<	
17+Cl	0,0766	0,0085	39+Y2O3	<		76 OsO4	<	
18+Ar	0,0071	0,0021	40+ZrO2	0,0377	0,0019	77 IrO2	<	
19+K2O	3,69	0,21	41 Nb2O5	<		78 PtO2	<	
20+CaO	7,8	0,3	42+MoO3	<		79 Au	<	
21 Sc2O3	<		44+RuO2	<		80 HgO	<	
22+TiO2	0,724	0,08	45+Rh2O3	<		81 Tl2O3	<	
23+V2O5	0,0172	0,0014	46+PdO	<		82 PbO	<	
24+Cr2O3	0,0186	0,0021	47 Ag2O	<		83 Bi2O3	<	
25+MnO	0,099	0,005	48 CdO	<		90 ThO2	<	
26+Fe2O3	6,31	0,27	49 In2O3	<		92 U3O8	<	
27 Co3O4	<		50 SnO2	<		94 PuO2	<	
28+NiO	<		51 Sb2O3	<		95 Am2O3	<	

==== Light Elements =====			==== Noble Elements =====			===== Lanthanides =======		
SumBe..F	0,192	0,031	44+RuO2	<		57+La2O3	0,0063	0,0016
4 BeO	<		45+Rh2O3	<		58 CeO2	<	
5 B2O3	<		46+PdO	<		59 Pr6O11	<	
6 CO2	<		47 Ag2O	<		60 Nd2O3	<	
7 N	<		75 Re2O7	<		62+Sm2O3	<	
8 O	<		76 OsO4	<		63 Eu2O3	<	
9+F	0,192	0,031	77 IrO2	<		64 Gd2O3	<	
			78 PtO2	<		65+Tb4O7	<	
			79 Au	<		66 Dy2O3	<	
						67 Ho2O3	<	
						68+Er2O3	<	

						69 Tm2O3	<	
						70 Yb2O3	<	
						71 Lu2O3	<	

Sample 5, Black shale

R.M.S.	0.000
Sum before normalization	96.0 %
Normalised to	100.0 %
Sample type	Solid
Correction applied for medium	No
Correction for film	None
Used compound list	OXIDES
Results database	24cr
Results database in	c:\program files\panalytical\superq\userdata

Analyte	**Calibration status**	**Compound formula**	**Concentration (%)**	**Calculation method**
Rb	Calibrated	Rb2O	0.017	Calculate
		C5H8O2	5.901	Fixed
Na	Calibrated	Na2O	0.575	Calculate
Al	Calibrated	Al2O3	19.865	Calculate
Si	Calibrated	SiO2	57.716	Calculate
P	Calibrated	P2O5	0.144	Calculate
S	Calibrated	SO3	0.107	Calculate
K	Calibrated	K2O	3.736	Calculate
Ti	Calibrated	TiO2	1.025	Calculate
Mn	Calibrated	MnO	0.124	Calculate
Fe	Calibrated	Fe2O3	6.345	Calculate
Ni	Calibrated	NiO	0.014	Calculate
Cu	Calibrated	CuO	0.032	Calculate
Zn	Calibrated	ZnO	0.018	Calculate
Sr	Calibrated	SrO	0.015	Calculate
Y	Calibrated	Y2O3	0.007	Calculate
Zr	Calibrated	ZrO2	0.017	Calculate
Ba	Calibrated	BaO	0.039	Calculate
Ce	Calibrated	CeO2	0.028	Calculate
Cl	Calibrated	Cl	0.032	Calculate
Sc	Derived	Sc2O3	0.003	Calculate
Ca	Calibrated	CaCO3	0.644	Calculate
Mg	Calibrated	MgCO3	3.596	Calculate